

# The Global Climate and Atmospheric Dynamics of Extrasolar Lava Planets



Mark Hammond  
Hertford College  
University of Oxford

A thesis submitted for the degree of  
*Doctor of Philosophy*  
Michaelmas Term 2019

Dedicated to whomever

## Acknowledgements

Lorem ipsum dolor sit amet, consectetuer adipiscing elit. Ut purus elit, vestibulum ut, placerat ac, adipiscing vitae, felis. Curabitur dictum gravida mauris. Nam arcu libero, nonummy eget, consectetuer id, vulputate a, magna. Donec vehicula augue eu neque. Pellentesque habitant morbi tristique senectus et netus et malesuada fames ac turpis egestas. Mauris ut leo. Cras viverra metus rhoncus sem. Nulla et lectus vestibulum urna fringilla ultrices. Phasellus eu tellus sit amet tortor gravida placerat. Integer sapien est, iaculis in, pretium quis, viverra ac, nunc. Praesent eget sem vel leo ultrices bibendum. Aenean faucibus. Morbi dolor nulla, malesuada eu, pulvinar at, mollis ac, nulla. Curabitur auctor semper nulla. Donec varius orci eget risus. Duis nibh mi, congue eu, accumsan eleifend, sagittis quis, diam. Duis eget orci sit amet orci dignissim rutrum.

## **Abstract**

This thesis aims to understand the global circulation of tidally locked lava planets, and how to interpret observations of them.

# *Contents*

---

<b>1</b>	<b>Introduction</b>	<b>1</b>
<b>2</b>	<b>Tidally Locked Lava Planets and 55 Cancri e</b>	<b>6</b>
2.1	Exoplanets . . . . .	7
2.2	Lava Planets . . . . .	9
2.2.1	Tidally Locked Planets . . . . .	9
2.2.2	The Atmospheric Circulation of Tidally Locked Planets . . . . .	10
2.2.3	Lava Planets . . . . .	10
2.3	55 Cancri e . . . . .	10
<b>3</b>	<b>Wave-Mean Flow Interactions in a Linear Theory of Tidally Locked Atmospheres</b>	<b>12</b>
3.1	The Shallow-Water Equations . . . . .	15
3.1.1	Free Solutions . . . . .	16
3.1.2	Forced Solutions . . . . .	17
3.1.3	Wave Interactions with Flow . . . . .	20
3.2	Zonal Acceleration . . . . .	21
3.2.1	Acceleration in a Matsuno-Gill Model . . . . .	21
3.2.2	Correction to Vertical Momentum Transport . . . . .	23
3.2.3	Equilibrium Equatorial Flow . . . . .	25
3.2.4	Horizontal Momentum Transport from Stationary Waves . . . . .	26
3.2.5	Horizontal Momentum Transport from Transient Waves . . . . .	26
3.3	Wave Interactions with Shear Flow on the Beta-Plane . . . . .	26
3.3.1	Free Modes . . . . .	30
3.3.2	Forced Solutions . . . . .	33
3.3.3	Equilibrium Circulation . . . . .	33
3.3.4	Damping . . . . .	35

3.3.5	Hot-Spot Shift . . . . .	36
3.4	Wave Interactions with Shear Flow on a Sphere . . . . .	36
3.4.1	Spherical Shallow-Water Equations . . . . .	36
3.4.2	Forced Solutions . . . . .	36
3.5	Scaling Relations . . . . .	36
3.5.1	1D Scaling Relations . . . . .	36
3.5.2	2D Scaling Relations . . . . .	36
3.6	Other Jet Patterns . . . . .	36
<b>4</b>	<b>Equilibrium Circulation States on Tidally Locked Planets</b>	<b>38</b>
4.1	Equilibrium Flow Profile . . . . .	38
4.2	Initial Conditions . . . . .	40
4.3	Instabilities as deviations from equilibrium . . . . .	40
4.4	Jet Scaling Relations . . . . .	40
<b>5</b>	<b>Non-Linear Tests of a Linear Theory of Tidally Locked Atmospheres</b>	<b>41</b>
5.1	Non-Linear Tests of Linear Shallow-Water Theory . . . . .	42
5.2	GCM Tests of Shallow-Water Theory . . . . .	49
<b>6</b>	<b>Linking the Climate and Thermal Phase Curve of 55 Cancri e</b>	<b>51</b>
6.1	Observations of 55 Cancri e . . . . .	53
6.2	Simulating a Lava Planet . . . . .	58
6.3	Simplified Scaling Theory . . . . .	61
6.4	Results . . . . .	67
6.4.1	Effect of Mean Molecular Weight . . . . .	70
6.4.2	Effect of Surface Pressure . . . . .	72
6.4.3	Effect of Optical Thickness . . . . .	74
6.4.4	Vertical Structure . . . . .	75
6.4.5	Mean Molecular Weight . . . . .	79
6.4.6	Surface Pressure . . . . .	79
6.4.7	Optical Thickness . . . . .	79
6.4.8	Vertical Structure . . . . .	79
6.4.9	Phase Curves . . . . .	79
6.5	Simulated Observations . . . . .	79
6.5.1	Condensables and Clouds . . . . .	82
6.6	Discussion . . . . .	84
6.7	Conclusions . . . . .	87

<b>7</b>	<b>Clouds on Lava Planets</b>	<b>91</b>
7.1	Clouds on Lava Planets . . . . .	92
7.2	Methods . . . . .	92
7.2.1	SOCRATES Radiative Transfer . . . . .	92
7.2.2	DIHRT Dynamical Clouds . . . . .	92
7.3	Cloud-Free Simulation . . . . .	92
7.3.1	Observations . . . . .	92
7.4	Simulations . . . . .	92
7.4.1	Pure CO Atmosphere . . . . .	92
7.4.2	Pure CO Atmosphere with Na . . . . .	92
7.4.3	Pure CO Atmosphere with H <sub>2</sub> O . . . . .	92
7.4.4	H <sub>2</sub> Atmosphere . . . . .	92
7.5	Discussion . . . . .	92
7.5.1	Implications for Climate . . . . .	92
7.5.2	Implications for Observations . . . . .	92
<b>8</b>	<b>Comparing Lava Planets</b>	<b>93</b>
8.1	55 Cancri e . . . . .	94
8.2	K2-141b . . . . .	94
8.3	LHS 3844b . . . . .	94
<b>9</b>	<b>Conclusions</b>	<b>95</b>
<b>Bibliography</b>		<b>96</b>
<b>A</b>	<b>Exo-FMS</b>	<b>98</b>
A.1	Model Structure . . . . .	99
A.2	Dynamics . . . . .	99
A.3	Radiative Transfer . . . . .	100
A.4	Cloud Microphysics . . . . .	100
A.5	Example Planets . . . . .	100
A.5.1	Temperate Terrestrial Planets . . . . .	100
A.5.2	Lava Planets . . . . .	100
A.5.3	Gas Planets . . . . .	100
<b>B</b>	<b>GFDL-SDC</b>	<b>101</b>
B.1	Model Details . . . . .	101
B.2	Simulation Details . . . . .	101

<b>C Pseudo-Spectral Methods</b>	<b>103</b>
C.1 Solving Equations . . . . .	104
C.2 Example Solutions . . . . .	107

## *List of Figures*

---

1.1	The population of known exoplanets plotted by semi-major axis and stellar mass. All the planets below the line have a timescale to reach a tidally locked state of less than 0.1 billion years, so are expected to be in this state. . . . .	3
3.1	Example GCM results. . . . .	13
3.2	Free Modes. . . . .	17
3.3	Forced solutions. . . . .	19
3.4	Acceleration terms. . . . .	22
3.5	Acceleration terms with R. . . . .	24
3.6	Eigenvalue shift. . . . .	29
3.7	The meridional structure of the free Kelvin mode. . . . .	29
3.8	The meridional structure of the free Rossby mode ( <a href="#">Hammond and Pierrehumbert, 2018</a> ). . . . .	30
3.9	Zero Flow and Shear Flow. . . . .	34
3.10	Acceleration versus speed. . . . .	34
3.11	Zero Flow and Shear Flow. . . . .	35
3.12	Explanation. . . . .	35
3.13	Forced linear shallow-water solutions in spherical geometry with and without background shear flows. The parameters of the model are $\tilde{U} = 0.5 \cos \phi \exp(-(\phi/\phi_0)^2)$ , $\phi_0 = \pi/3$ , $\alpha_{dyn} = \alpha_{rad} = 0.2$ , $G = 1$ , $Q = 0.5 \cos(\phi)$ , as discussed in Section ??.	37

---

## List of Figures

5.1	The linear response. . . . .	43
5.2	5e3. . . . .	45
5.3	Nonlinear. . . . .	45
5.4	Matsuno jet control. . . . .	46
5.5	Nonlinear with and without imposed jet. . . . .	47
6.1	Phase curve. . . . .	54
6.2	Temperature map. . . . .	55
6.3	Our parameter space, where the green region is the regime predicted to support both a significant hot-spot shift and day-night contrast. The black points show the atmospheres we tested, detailed in Table 6.4. We used a fixed advection speed $1000 \text{ ms}^{-1}$ and fixed mean temperature $2000\text{K}$ . The lines correspond to a predicted hot-spot shift of $20$ <i>and a day-night contrast of 80% of the equilibrium contrast (with no heat transport). We tested some over</i>	68
6.4	$\tau_\infty$ – in our parameter space, we do not expect it to affect the hot-spot shift or fractional day-night contrast (see Sections ?? and 6.4.3). . . . .	68
6.5	10-day average temperature maps centred on the substellar point, after each Exo-FMS test reaches top-of-atmosphere radiative balance. The first column is surface air temperature, which generally shows the largest day-night contrast as it is strongly coupled to the surface temperature and incoming stellar flux. The second column is the half-pressure air temperature, which generally shows the largest hot-spot shift as it is normally close to the height of the superrotating jet. The third column is the brightness temperature, which determines the thermal phase curve for the model grey-gas radiation – in reality, the thermal emission could be from a different level of the atmosphere. . . . .	70
6.6	10-day average temperature maps of the half-surface-pressure level for $4.6 \text{ gmol}^{-1}$ and $15 \text{ gmol}^{-1}$ $\text{H}_2 + \text{N}_2$ atmospheres with surface pressures of 3, 5, and 10 bar, and constant opacity $\kappa = 22.4 \text{ cm}^2\text{kg}^{-1}$ . The global temperature distributions are similar but the maximum and minimum temperatures differ.	73
6.7	10-day average temperature maps of the half-surface-pressure level for $4.6 \text{ gmol}^{-1}$ $\text{H}_2 + \text{N}_2$ atmospheres with surface pressure 5 bar and optical thicknesses of 2.0, 4.0, and 8.0. . . . .	74

6.7	Vertical structure of the tested atmospheres. The best-fit “H <sub>2</sub> +N <sub>2</sub> , 5 bar” case here has mean molecular weight 4.6 gmol <sup>-1</sup> and $\tau_{\infty} = 4.0$ . The T(p) profiles follow the dry adiabat on the lower atmosphere of the day-side, but tend towards isothermal elsewhere. The day-night contrast always increases closer to the surface. The hot-spot shift generally increases further from the surface, but becomes indistinct without a large day-night contrast. . . . .	76
6.8	Phase curves for different radiating levels in the 5 bar, 4.6 gmol <sup>-1</sup> , H <sub>2</sub> + N <sub>2</sub> atmosphere. Raising the radiating level has a very similar effect to decreasing the molar mass in Figures ?? and ??, leading to a degeneracy in interpreting the observed phase curve (the black point and line show the maximum and minimum observed fluxes, with error bars). . . . .	77
6.9	Phase curves calculated using the emission from the half-surface-pressure level of the 4.6 gmol <sup>-1</sup> H <sub>2</sub> + N <sub>2</sub> atmospheres with surface pressures of 3, 5, and 10 bar, corresponding to the temperature maps in Figure 6.5. . . . .	80
6.10	Phase curves calculated using the emission from the half-surface-pressure level of the 5 bar 4.6 gmol <sup>-1</sup> H <sub>2</sub> + N <sub>2</sub> atmospheres with optical thicknesses of 2.0, 4.0, and 8.0, corresponding to the temperature maps in Figure 6.6. . . .	81
6.11	Simulated 4.5 phase curves calculated from the brightness temperature of the grey-gas OLR. The red curve is the 10 bar H <sub>2</sub> atmosphere, which has such efficient heat transport that it has a large peak offset and very small amplitude. The blue curve is the 10 bar N <sub>2</sub> atmosphere, with very weak heat transport so a large amplitude and peak offset. The green curve is the 5 bar H <sub>2</sub> +N <sub>2</sub> atmosphere, with a significant offset and amplitude. The offset and amplitude are not as large as the ? measurements, shown by the black point and line (with their errors shown by the bars and the shaded area). . . . .	82
6.12	Simulated phase curves for the emission from a radiating level at half-surface-pressure. The amplitude and offset are larger than the phase curves of the OLR. The offset and amplitude are not as large as the ? measurements, but Figure ?? shows that the H <sub>2</sub> +N <sub>2</sub> atmosphere (blue curve) could match the observations with the night-side cloud formation discussed in Section 6.5.1. . . . .	82

6.13 Simulated phase curves for different equilibrium surface partial pressures of SiO in the $4.6 \text{ gmol}^{-1}$ , 5 bar $\text{H}_2 + \text{N}_2$ atmosphere. 10 mbar corresponds to the mean day-side surface temperature, 50 mbar to the mean temperature in the region between 25N to 25S and 25E to 25W, and 100 mbar to the maximum surface temperature. The 300 mbar curve shows that clouds could form on the day-side at high enough surface partial pressures. The offset and amplitude of the 100 mbar case almost agrees with the ? measurements within error. It is not clear which partial pressure is appropriate, as the calculated pressures strictly apply to magma under a vacuum (?), and there is not a single clear magma ocean temperature in our results. . . . .	85
C.1 Basis functions used in beta-plane and spherical coordinates. . . . .	107
C.2 Coefficients of the pseudo-spectral solution on the beta-plane coordinates with and without a background jet (the plots in Figure ??). The method identifies the exact solution in the first case, and converges rapidly to an accurate solution in the second case. . . . .	109
C.3 Coefficients of the pseudo-spectral solution in spherical coordinates (the first plot in Figure 3.13), with the height variable $h$ and the rescaled height $y$ . Rescaling the height makes the method converge to a smooth solution at the poles. . . . .	110

# CHAPTER 1

## *Introduction*

---

*“Any finite number divided by infinity is as near to nothing as makes no odds, so the average population of all the planets in the Universe can be said to be zero. From this it follows that the population of the whole Universe is also zero, and that any people you may meet from time to time are merely the products of a deranged imagination.”*

— Douglas Adams, *The Restaurant at the End of the Universe*

Lava planets are rocky, very hot, and orbit so close to their host stars that they are expected to be tidally locked to them. This means that they always present the same side to the star, so have a permanent day-side and night-side. This thesis investigates the question of what these properties mean for the atmosphere of the planet, particularly its circulation and composition. Tidally locked planets are very common and observable. Lava planets are particularly observable, especially for rocky planets.

Why are tidally locked planets important? Their unusual situation could make them seem like oddities, unrelated to the majority of planets. On the contrary, Figure 1.1 shows that a large fraction of known exoplanets are expected to be tidally locked. It shows the stellar masses and semi-major axes for all exoplanets listed on the NASA Exoplanet Archive

---

at the time of writing, with all the planets below the line expected to be tidally locked  
([Pierrehumbert and Hammond, 2018](#)).

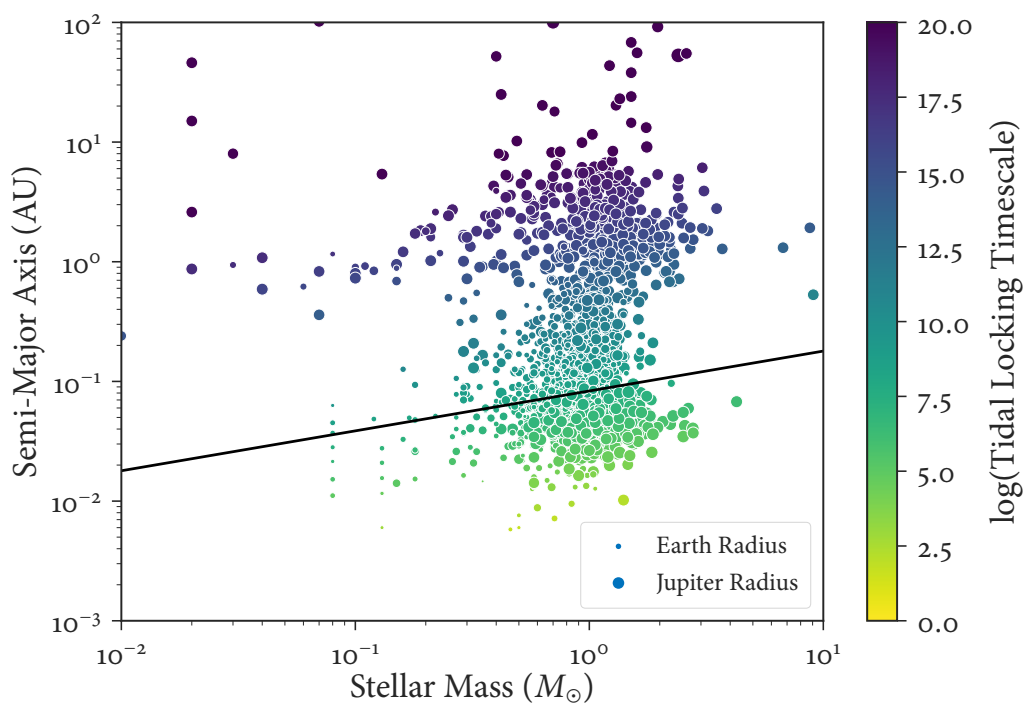


Figure 1.1: The population of known exoplanets plotted by semi-major axis and stellar mass. All the planets below the line have a timescale to reach a tidally locked state of less than 0.1 billion years, so are expected to be in this state.

---

These planets are also generally more easily characterised than the others, giving larger signals for spectroscopy when they transit their stars. This tendency may have created a detection bias, where close-in exoplanets are more likely to be detected so it appears that a greater fraction are tidally locked than is actually the case. Even if this is true, it does not detract from the relevance of tidally locked planets – we can only study planets we know about!

In Chapter 1, I discuss the concept of a “lava planet” and review the literature of discovery, characterisation, and modelling of such planets. I aim to introduce the scientific concepts and questions that I will address through the rest of the thesis.

In Chapter 2, I discuss the theoretical work I did to understand the global circulation of tidally locked planets in general. In the course of trying to understand simulations of tidally locked lava planets, we found that there was not a full understanding of key features of their circulation. I explain how I used a two-dimensional model to represent the atmosphere of a tidally locked planet, and demonstrated that the equatorial jet that forms affects the global circulation and temperature pattern. This was key to our work on lava planets, but was applicable to any tidally locked planet.

### Chapter 3 follows Chapter 2

In Chapter 3, I introduce the model I used to simulate three-dimensional planetary atmospheres, the General Circulation Model (GCM) Exo-FMS. Developing this model formed a large part of the work of my DPhil. I discuss the structure I developed, and the physical processes represented within it. I focus on the particular challenges of simulating tidally locked lava planets, and defer many technical details to Appendix A.

In Chapter 4, I discuss my first project using the simulations discussed in Chapter 3, to

---

interpret observations of a lava planet.

Chapter 5 follows Chapter 4, and shows how in collaboration with Graham Lee we simulated dynamic, radiatively active clouds on 55 Cancri e in order to answer the questions raised by Chapter 4 on the effect of clouds in its atmosphere.

In the Conclusion, I summarise my work on the global circulation of tidally locked planets, and its relevance for 55 Cancri e.

## CHAPTER 2

# *Tidally Locked Lava Planets and 55 Cancri e*

---

*“One face is forever sunlit, and one forever dark, and only the planet’s slow liberation gives the twilight zone a semblance of seasons.”*

— Stanley G. Weinbaum, *The Lotus Eaters*

Perhaps the most exciting discovery from the field of exoplanet science is that other stars host planets which are very different from those in our solar system. There are similar planets to those in the solar system – “Hot Jupiters”, high-temperature Jupiter-sized gas giants in short-period orbits, or “Mini-Neptunes”, which show the literal-mindedness of planetary scientists. But some exoplanets have no analogues in the solar system, and “lava planets” are some of the best examples of these.

This short chapter describes the class of “lava planets”, particularly the planet 55 Cancri e, and discusses the question that this thesis aims to answers about this planet.

I will describe lava planets in general, and list the known planets in this class. I will then discuss the 55 Cancri system, and the lava planet 55 Cancri e in that system.

I will try to show that lava planets are a potentially bountiful area for scientific work, being interesting systems that have observational advantages. I will set up the question of the atmosphere and atmospheric circulation of 55 Cancri e, and show how it relates to the broader question of the nature of the climate of tidally locked planets.

## 2.1 Exoplanets

Exoplanets are planets orbiting stars other than our Sun. As far as we know, there is nothing fundamental to distinguish the planets in our Solar System from those elsewhere, so it is possible that this specific nomenclature may eventually disappear. I will use the word “exoplanet” when discussing specific planets or issues related to their distance, and “planet” in a more general or idealised context (such as the first sentence of this paragraph).

There is no better way to date a piece of writing on exoplanets than by announcing how many have been discovered, so I will just note that we know of several thousand and anticipate many more to come. The number of exoplanets which are favourable for detailed observations is still quite small, and we can observe atmospheric details for perhaps only a few dozen planets. In fact, while the title of this thesis suggests it looks at “lava planets”, there is really only one that is currently observable – 55 Cancri e. Despite this, I hope to draw general conclusions about the circulation of many types of planet, and contribute to an understanding of tidally locked planets and lava planets for future observations.

## Discovering Exoplanets

This is not a thesis on discovering exoplanets, although the methods of discovery are sometimes relevant to the characterisation that is of interest. Most exoplanets discovered to date have been found using either a “radial velocity” method or a “transit” method.

In the first method, the motion of a star around its common center of mass with a planet orbiting it is detected by measuring the Doppler-shift of emission lines of the star. The magnitude and period of this motion gives the period of the planet’s orbit, and a limit on its mass.

In the second method, a planet passing across the line of sight from an observer to the star produces a dip in the light seen by the observer. A periodic dip gives the period of the planet, and the size of the dip gives its radius. So, if a planet can be measured with both methods the observer retrieves its period, mass, radius, density, semi-major axis, and equilibrium temperature.

## Characterising Exoplanets

This is also not a thesis on characterising exoplanets, although I have tried to keep observations in mind throughout the simulations and theory.

The atmospheres of exoplanets can be characterised through transmission and emission spectroscopy. In transmission spectroscopy, light from the host star passes through the atmosphere of the exoplanet before it reaches the observer, and the spectrum is measured. An alternative (but equivalent) view is that the planet appears to have a different radius as it transits its star at different wavelengths – at a wavelength the atmosphere is

more opaque to, the planet appears larger – so the absorption spectrum of the gases in the atmosphere can be retrieved.

In emission spectroscopy, the spectrum of the light emitted thermally by the planet and its atmosphere is measured. Hotter planets emit more light in this way, so are better suited to this method.

## 2.2 Lava Planets

### 2.2.1 Tidally Locked Planets

A tidally locked planet, or a “synchronously rotating” planet, always presents the same face to the star it orbits, as its rotation period is the same as its orbital period. An asynchronously rotating planet like the Earth has a different rotation period (1 day) to its orbital period (1 year). Tidal forces slow down the rotation of such planets, until they become tidally locked. The time for a planet to become tidally locked is approximately:

See Chapter 3 for an investigation of the atmospheric dynamics of tidally locked planets.

Tidally locked planets include Hot Jupiters, Earth-like planets like those in the Trappist-1 system, and lava planets like 55 Cancri e, discussed next.

### 2.2.2 The Atmospheric Circulation of Tidally Locked Planets

### 2.2.3 Lava Planets

“Lava Planets” are terrestrial (rocky, not gaseous) planets orbiting very close to their parent star.

## 2.3 55 Cancri e

55 Cancri e is a tidally locked lava planet orbiting the binary star 55 Cancri, 41 light years away in the constellation of Cancer.

### The 55 Cancri system

Figure X shows the 55 Cancri system.

### 55 Cancri e

55 Cancri e is the closest planet to the G-star 55 Cancri A.

### A Thermal Phase Curve of 55 Cancri e

A phase curve is the light measured from a planet as it orbits its star. They are particularly useful for tidally locked planets. Figure X shows a phase curve for X.

A thermal phase curve refers to the light emitted by the planet itself, rather than the light it reflects from the star it orbits. For a tidally locked planet, the thermal phase curve

shows the hemisphere-averaged brightness temperature of the planet as it rotates.

[Demory et al. \(2016\)](#) measured a thermal phase curve of the planet 55 Cancri e.

55 Cancri e is currently the most easily observable terrestrial tidally locked planet. Its composition, atmosphere, and circulation provide tests of theories of planet formation and atmospheric dynamics. In this thesis, I will use it as a case study for the atmospheric dynamics of tidally locked planets.

## CHAPTER 3

# *Wave-Mean Flow Interactions in a Linear Theory of Tidally Locked Atmospheres*

---

“One might as well approximate the derivatives well instead of badly”

— John P. Boyd, *Chebyshev and Fourier Spectral Methods*

Tidally locked planetary atmospheres have such a different spatial energy input to planets like the Earth that it is not obvious that conventional Earth-like atmospheric dynamics should be able to describe them. However, the planetary-scale day-night forcing difference makes the global circulation highly susceptible to a simple shallow-water model, compared to the higher order effects controlling the Earth’s atmosphere.

This chapter discusses my work using a single-layer linear shallow-water model to investigate the global circulation of tidally locked planets. It follows directly from the work of XX and XX. As introduced in Chapter 2, the atmospheres of tidally locked planets are understood to generally have a strong eastward equatorial jet, a hot-spot shifted eastward of their substellar point, and a pair of cold low-pressure lobes on their night-side. Figure 3.1 shows a GCM simulation of a tidally locked planet with Earth-like size and instellation,

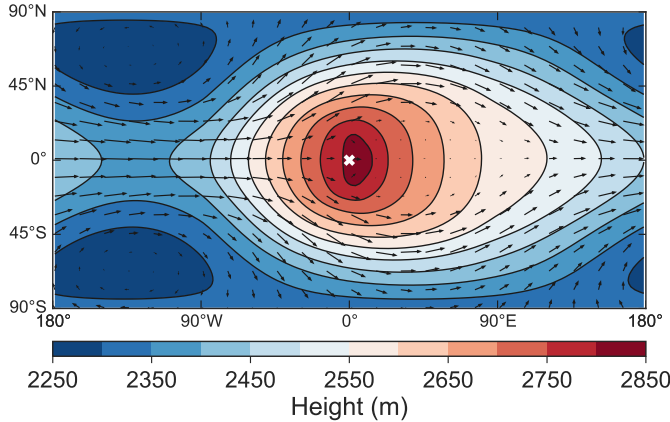


Figure 3.1: Example GCM results.

showing these features.

In this chapter, I will show that the interaction of this mean zonal flow and the standing waves produced by the stationary day-night forcing is crucial to the global circulation of tidally locked planets. [Showman and Polvani \(2011\)](#) used a shallow-water model to model the standing waves on tidally locked planets, and to explain the equatorial superrotation. However, the equilibrium state of their shallow-water model only matched the form of their GCM simulations over the first few days after spin-up from rest. [Tsai et al. \(2014\)](#) suggested that this was because the zonal flow shifted the standing wave response eastwards, and used a uniform flow (with no height perturbation) in a shallow-water model to show this. In this chapter, I follow both of these studies and linearise the shallow-water equations around a meridionally sheared zonal flow  $\bar{U}(y)$  with an associated height perturbation  $\bar{H}(y)$ . I show that the response to day-night forcing in this system matches GCM simulations of tidally locked planets, particularly the form of the hot-spot shift and the cold

---

lobes on the night-side.

After introducing the linear shallow-water model and the work of Matsuno, Gill, Showman, and Tsai, I will show how I linearised the model about a zonally uniform jet  $\bar{U}(y)$  with latitudinal shear, as well as its associated geostrophic height perturbation  $\bar{H}(y)$

In Section 1, I will introduce the system of shallow-water equations on a rotating beta-plane, and discuss the response to a day-night forcing, in zero background flow and in uniform background flow (an approximation to the later shear flow and height perturbation).

In Section 2, I will show the zonal acceleration produced by this forced response, discussing how [Showman and Polvani \(2010\)](#) showed that a correction to the classical model of [Matsuno \(1966\)](#) is required to produce equatorial superrotation.

In Section 3, I will linearise the beta-plane shallow-water equations about a background flow  $\bar{U}(y)$  and associated height perturbation  $\bar{H}(y)$ , representing the flow produced by this acceleration. I will find the free modes of this system and the response to the same day-night forcing as before. This will show that the forced response is shifted eastwards, combining with the zonally uniform jet perturbation to produce the global circulation pattern seen in GCM simulation and hinted at by observations.

In Section 4, I will show the same calculation for the shallow-water equations on a sphere, which have less intuitive solutions but are more directly comparable to real planets and GCM simulations.

In Section 5, I will use the shallow-water equations to produce simple one-dimensional scaling relations for the height field along the equator, and compare them to the two-dimensional scaling relations predicted by the solutions in the previous sections.

In the next chapters, I will return to these stationary solutions and scaling relations to compare them to GCM simulations.

I will show that linearising the jet about the shear flow and its height perturbation makes the forced linear response match nonlinear GCM simulations much more closely. The new model reveals scaling relations between the planetary parameters such as forcing strength, and the observable quantities such as the eastward hot-spot shift.

This chapter is based on work produced for [Hammond and Pierrehumbert \(2018\)](#). Some of the figures, which I generated, have been taken directly from this paper. None of the text has been reused, and the structure is significantly different.

### 3.1 The Shallow-Water Equations

We used the linear shallow-water equations on a one-layer equatorial beta-plane to model the atmosphere of a tidally locked planet. These equations describe the motion of a single layer of fluid of constant density where the horizontal scale of its flow is much greater than the depth of the fluid. The linear form of these equations describe small perturbations to this layer ([Vallis, 2006](#)). We model the atmosphere of a tidally locked planet with a similar shallow-water model to [Showman and Polvani \(2011\)](#). The model corresponds to an active upper layer following the single-layer shallow water equations, above a quiescent layer which can transport mass and momentum to and from the upper layer. The forcing due to stellar heating is represented by  $Q$ , a relaxation to the radiative equilibrium height field.

### 3.1.1 Free Solutions

In this section, we derive the wave response to stationary forcing on the beta-plane ([Matsuno, 1966](#)). The beta-plane system approximates the Coriolis parameter as linear, which is only accurate at low latitudes but leads to more intuitive and useful solutions than the full spherical geometry. We solve the equations in a spherical geometry in Section ??, and show that the beta-plane approximation leads to very similar solutions, as in other studies of the atmospheres of tidally locked planets ([Showman and Polvani, 2011](#)) ([Heng and Workman, 2014](#)).

All the quantities are linearized as the sum of a zonally mean background value  $F(y)$  and a perturbation with the form  $f(y)e^{i(k_x x - \omega t)}$  (unlike [Matsuno \(1966\)](#), who uses the less conventional form  $f(y)e^{i(k_x x + \omega t)}$ ). Throughout this paper, we will use capital letters for mean zonal quantities such as  $\bar{U}$  and  $\bar{H}$ , and lower-case letters for perturbations to this background, such as  $u$  and  $h$  (unless otherwise specified, such as the forcing  $Q$ ). The shallow-water equations for these perturbations with zero background flow are:

$$\begin{aligned} \frac{\partial u}{\partial t} - \beta y v + \frac{\partial h}{\partial x} &= 0 \\ \frac{\partial v}{\partial t} + \beta y u + \frac{\partial h}{\partial y} &= 0 \\ \frac{\partial h}{\partial t} + c^2 \left( \frac{\partial u}{\partial x} + \frac{\partial v}{\partial y} \right) &= Q(x, y) \end{aligned} \quad (3.1)$$

where  $h$  is the height,  $c = \sqrt{gH}$  is the gravity wave speed ([Matsuno, 1966](#)), and there is no friction or damping. Non-dimensionalizing with time scale  $\sqrt{1/c\beta}$  and length scale  $\sqrt{c/\beta}$  (the equatorial Rossby radius of deformation  $L_R$ ), and assuming all quantities have the form  $f(y)e^{i(kx - \omega t)}$ , the free equations with zero forcing are:

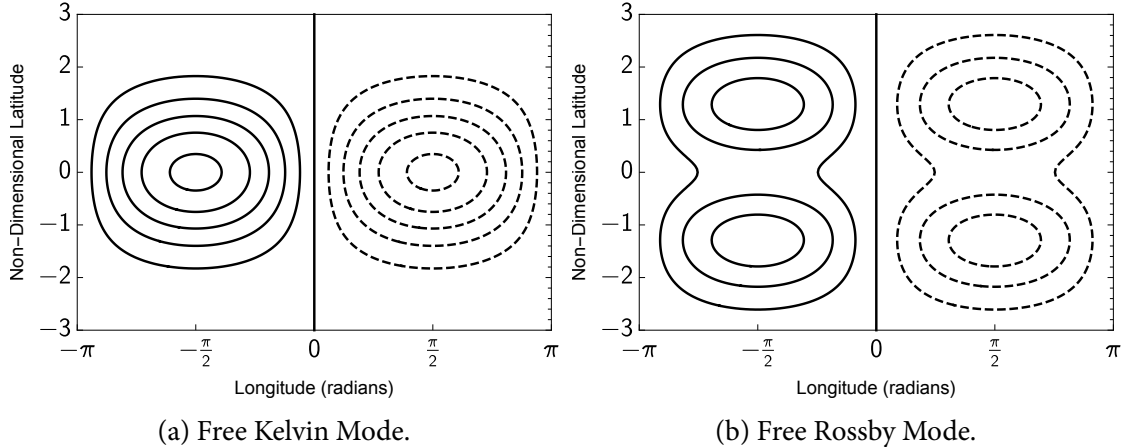


Figure 3.2: Free Modes.

$$\begin{aligned}
 -i\omega u - yv + ik_x h &= 0 \\
 -i\omega v + yu + \frac{\partial h}{\partial y} &= 0 \\
 -i\omega h + iku + \frac{\partial v}{\partial y} &= 0
 \end{aligned} \tag{3.2}$$

Matsuno (1966) gives the free modes of this system as XX. Figure 3.2a shows the free Kelvin mode with wavenumber 1 and Figure 3.2b shows the free Rossby mode with wavenumber 1.

EIGENVALUES GIVE POSITION IN FORCED RESPONSE.

### 3.1.2 Forced Solutions

In this chapter, I will focus on the response of the shallow-water equations to a forcing  $Q(x, y)$  on the height field  $h$ , representing the stellar forcing on a tidally locked planet. The forced solution can be considered to be a sum of the free modes discussed in the previous

section, at different locations and with different strengths.

The forced equations are:

$$\begin{aligned}\alpha_{rad}u - \beta yv + \frac{\partial h}{\partial x} &= 0 \\ \alpha_{rad}u + \beta yu + \frac{\partial h}{\partial y} &= 0 \\ \alpha_{dyn}h + c^2\left(\frac{\partial u}{\partial x} + \frac{\partial v}{\partial y}\right) &= Q(x, y)\end{aligned}\quad (3.3)$$

with boundary conditions

$$u, v, h \rightarrow 0 \quad \text{for } y \rightarrow \pm\infty. \quad (3.4)$$

Matsuno (1966) shows how the response of Equation 3.3 to a forcing  $Q(x, y) = Q_0 \sin(x) e^{-y^2/2}$  and uniform damping  $\alpha_{rad} = \alpha_{dyn} = \alpha$  can be found analytically as a sum of the free modes of the system. The forced response  $\chi = (u, v, h)$  is a sum of the free modes  $\xi_m = (u_m, v_m, h_m)$ , weighted by coefficients  $a_m$

$$\chi = \sum a_m \xi_m, \quad (3.5)$$

where the coefficients are given by

$$a_m = \frac{1}{\alpha - i\omega_m} b_m, \quad (3.6)$$

where  $\omega_m$  is the eigenvalue of the mode  $m$ , and

$$b_m = \left[ \int \bar{\xi}_m(y) \sigma(y) dy \right] / \left[ \int |\xi_m(y)|^2 dy \right]. \quad (3.7)$$

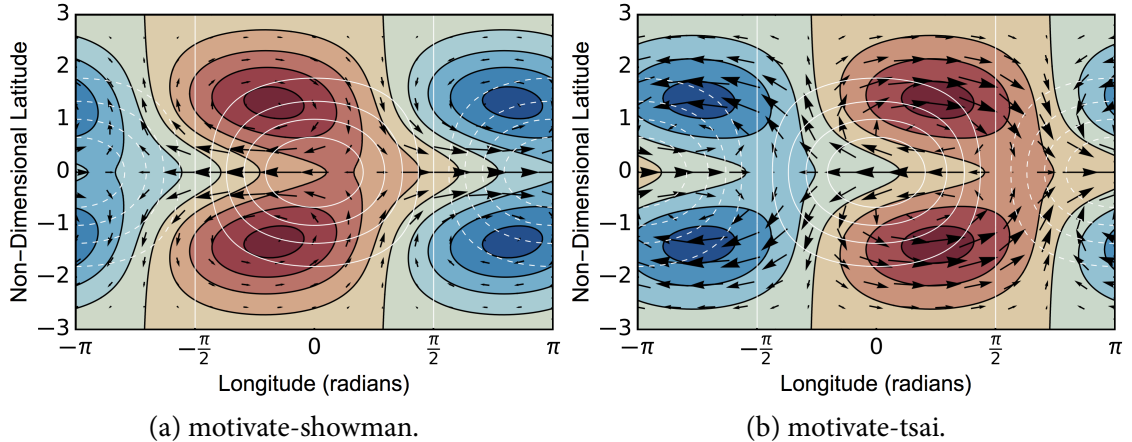


Figure 3.3: Forced solutions.

For the forcing  $Q(x, y) = Q_0 \sin(x) e^{-y^2/2}$ , all of the coefficients  $a_m$  are zero, apart from those for the Kelvin wave and the  $n = 1$  Rossby wave. Figure 3.3a shows this forced response.

**DO THIS!** The eigenvalues determine the position of each free mode in the forced response.

In the rest of this chapter, I will instead use the pseudo-spectral method described in Appendix C to find the response to forcing. This method works for any forcing and background flow (unlike the analytic method), and still finds the exact analytic solution for this case with zero background flow. Figure 3.3a was actually calculated using this pseudo-spectral method rather than expanding in terms of the free modes, but the solution is identical (as explained in Appendix C, the basis functions of the pseudo-spectral method can exactly represent the free modes of the shallow-water system).

### 3.1.3 Wave Interactions with Flow

This flow can be approximated as uniform, and the resulting solutions for the free and forced modes are only slightly modified from the case with zero flow.

Figure 3.3b shows the response of Equation 3.1 to a forcing  $Q(x, y) = Q_0 \sin(x) e^{-y^2/2}$ , with a uniform background flow  $\bar{U}(y) = U_0$ . [Tsai et al. \(2014\)](#) shows that there is still an analytic solution for the forced response in a uniform background flow, with a uniform background height field. All of the modes comprising the forced response are Doppler-shifted eastwards by the background flow.

DO THIS PART BELOW!

The modes present in the forced response are shifted significantly by a zonal flow of non-dimensional magnitude XX. This depends on the eigenvalue.

In this chapter, I will build on these solutions by linearising these shallow-water equations around a non-uniform equatorial jet  $\bar{U}(y)$  and its associated height perturbation  $\bar{H}(y)$ . This differs from [Showman and Polvani \(2011\)](#) which used zero background flow  $\bar{U}(y) = 0$  and uniform background height  $\bar{H}(y) = H_0$ . It also differs from [Tsai et al. \(2014\)](#) which used uniform background flow  $\bar{U}(y) = U_0$  and uniform background height  $\bar{H}(y) = H_0$  (which is inconsistent – a geostrophically balanced uniform flow  $\bar{U}(y) = U_0$  gives a non-uniform height field  $\bar{H}(y)$ ).

## 3.2 Zonal Acceleration

This shallow-water system shows which stationary waves will be excited in the atmosphere of a tidally locked planet by the day-night forcing. The next step is to calculate the zonal acceleration produced by these stationary waves, and find the effect of the resulting flow on the waves themselves.

I will follow [Showman and Polvani \(2010\)](#) and [Showman and Polvani \(2011\)](#) to show that the classic Matsuno-Gill model introduced in the previous section predicts zero acceleration at the equator. An addition momentum transport term is required to represent the asymmetric momentum forcing due to vertical transport on the day- and night-sides [Shell and Held \(2004\)](#).

### 3.2.1 Acceleration in a Matsuno-Gill Model

Zonally averaging the zonal momentum equation in Equation 3.1 ([Thuburn and Lagneau, 1999](#)) ([Showman and Polvani, 2010](#)) gives the zonal acceleration profile in the shallow-water model:

$$\frac{\partial \bar{u}}{\partial t} = \underbrace{\bar{v}^* \left[ f - \frac{\partial \bar{u}}{\partial y} \right]}_{I} - \underbrace{\frac{1}{\bar{h}} \frac{\partial}{\partial y} \left[ \overline{(hv)' u'} \right]}_{II} + \underbrace{\frac{1}{\bar{h}} \overline{u' Q'}}_{III} - \underbrace{\frac{\bar{u}^*}{\tau_{\text{drag}}}}_{IV} - \underbrace{\frac{1}{\bar{h}} \frac{\partial (\overline{h' u'})}{\partial t}}_{(3.8)}$$

Figure 3.4 shows the different components of Equation 3.8 for the classic system of [Matsuno \(1966\)](#):

- Green line: Term I, zonal momentum transport by mean meridional circulation

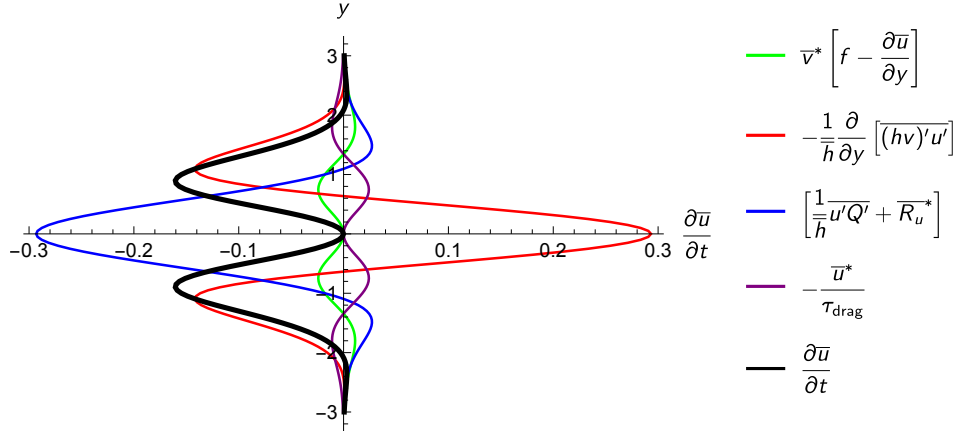


Figure 3.4: Acceleration terms.

- Red line: Term II, horizontal transport of zonal momentum
- Blue line: Term III, vertical transport of zonal eddy momentum
- Purple line: Term IV, zonal drag
- Black line: Left-hand-side, sum of all four terms.

Note that there is no contribution from the final term in Equation 3.8 as the solution is stationary.

The key point from Figure 3.4 is that there is zero zonal acceleration at the equator, so this model is not consistent with GCM simulations of tidally locked planets that show equatorial superrotation at the equator.

We can show that the acceleration must be zero at the equator for these forced shallow-water equations. Rewriting the zonal mean momentum equation in terms of the relative vorticity  $\zeta$  (Thuburn and Lagneau, 1999) (Showman and Polvani, 2011)

$$\frac{\partial \bar{u}}{\partial t} = \bar{v}' \bar{\zeta}' + \bar{v}(f + \bar{\zeta}) - \frac{\bar{u}}{\tau_{\text{drag}}} + \bar{R}_u, \quad (3.9)$$

we see that as  $v = 0$  at the equator (due to the symmetric forcing in  $y$ )  $\frac{\partial \bar{u}}{\partial t} = 0$  at the equator also.

The fact that there is in the GCM simulations shows another process is affecting the zonal momentum at the equator. Note that this condition still applies to the same equations linearised about a zonal flow  $\bar{U}(y)$  (Equation X).

### 3.2.2 Correction to Vertical Momentum Transport

The forced shallow-water equations predict zero zonal acceleration at the equator. So, there must be another process at work at the equator producing the eastward zonal flow seen in GCM simulations.

[Showman and Polvani \(2011\)](#) invoke a correction to the zonal momentum equation from [Shell and Held \(2004\)](#).

$$\begin{aligned} \frac{\partial u}{\partial t} - \beta y v + \frac{\partial h}{\partial x} &= R_u \\ \frac{\partial v}{\partial t} + \beta y u + \frac{\partial h}{\partial y} &= 0 \\ \frac{\partial h}{\partial t} + c^2 \left( \frac{\partial u}{\partial x} + \frac{\partial v}{\partial y} \right) &= Q(x, y) \end{aligned} \quad (3.10)$$

The correction  $R_u$  represents the effect of exchanging zonal momentum between the active layer and the lower layer. On the day-side, air with zero angular momentum rises from the substellar point into the active layer, giving a zonal acceleration which opposes the local  $u$  field. To conserve the vertically integrated local zonal momentum this acceleration

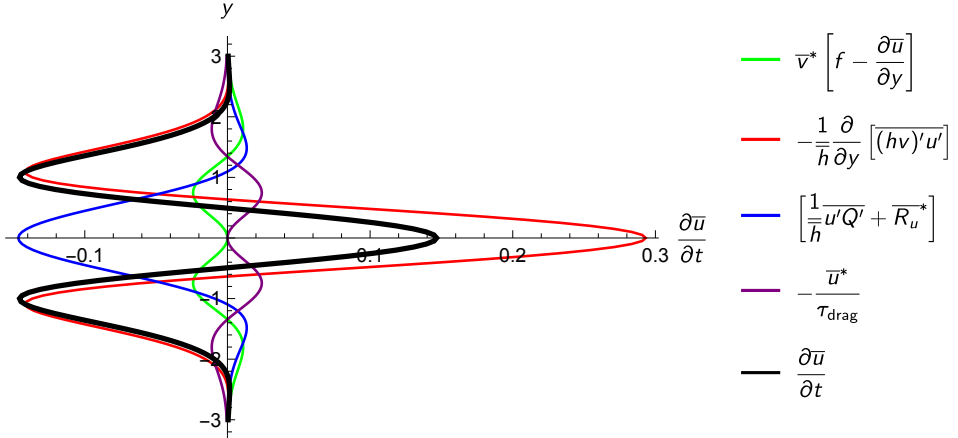


Figure 3.5: Acceleration terms with R.

is  $R_u - \frac{Qu}{h}$  (Showman and Polvani, 2011). On the night-side, air leaves the active layer which does not affect the local angular momentum, so  $R_u = 0$ .

$$R_u = \begin{cases} -\frac{Qu}{h}, & Q > 0 \\ 0, & Q < 0 \end{cases} \quad (3.11)$$

This modifies the zonal mean momentum equation to:

$$\frac{\partial \bar{u}}{\partial t} = \underbrace{\bar{v}^* \left[ f - \frac{\partial \bar{u}}{\partial y} \right]}_I - \underbrace{\frac{1}{h} \frac{\partial}{\partial y} \left[ (\bar{h}\bar{v})' \bar{u}' \right]}_II + \underbrace{\left[ \frac{1}{h} \bar{u}' \bar{Q}' + \bar{R}_u^* \right]}_{III} - \underbrace{\frac{\bar{u}^*}{\tau_{\text{drag}}} - \frac{1}{h} \frac{\partial (\bar{h}' \bar{u}')}{\partial t}}_{IV} \quad (3.12)$$

Figure 3.5 shows the terms Equation 3.12. In comparison to Figure 3.4, there is now a zonal acceleration at the equator.

Rewriting the zonal mean momentum equation in terms of the relative vorticity again shows that there is now a non-zero acceleration at the equator due to  $R_u$ :

$$\frac{\partial \bar{u}}{\partial t} = \bar{v}' \bar{\zeta}' + \bar{v}(f + \bar{\zeta}) - \frac{\bar{u}}{\tau_{\text{drag}}} + \bar{R}_u, \quad (3.13)$$

This explains the equatorial superrotation on tidally locked planets. But, it does not explain why momentum-conserving retrograde westward flow predicted by this shallow-water model in the mid-latitudes, does not appear in the GCM simulations, which instead have an atmosphere superrotating at most latitudes. In Chapter XX I will discuss this.

### 3.2.3 Equilibrium Equatorial Flow

This provides an estimate of the equilibrium zonal flow speed on the equator, which will occur when  $\frac{\partial \bar{u}}{\partial t} = 0$ :

$$\frac{\bar{u}}{\tau_{\text{drag}}} = \bar{R}_u, \quad (3.14)$$

As the zonal flow  $\bar{u}$  increases, the drag term  $\frac{\bar{u}}{\tau_{\text{drag}}}$  will increase until it balances the acceleration due to vertical momentum transport  $\bar{R}_u$ .

The acceleration due to vertical momentum transport  $\bar{R}_u$  will also decrease as the zonal flow  $\bar{u}$  increases, so even if  $\tau_{\text{drag}}$  is very large and  $\frac{\bar{u}}{\tau_{\text{drag}}}$  is negligible,  $\bar{R}_u$  will eventually become zero for large enough zonal flow, and the acceleration will become zero. [Showman and Polvani \(2011\)](#) suggest that  $\bar{R}_u$  simply gets smaller as the zonal mean  $\bar{u}$  gets larger. Later, I will add the fact that the forced response is Doppler-shifted eastwards, changing the part of the eddy response that is on the day-side and contributes to  $\bar{R}_u$ .

In addition, I will show how this eastward shift decreases term II in Equation 3.12 by shifting the different wave components closer together. This further decreases the equato-

### 3.3. Wave Interactions with Shear Flow on the Beta-Plane

---

rial acceleration as the zonal flow increases, making it reach an equilibrium sooner.

#### 3.2.4 Horizontal Momentum Transport from Stationary Waves

It is helpful to now consider the terms in Equation 3.8 in more detail.

Term II in Equation 3.8 is the horizontal momentum transport. The sign of Term II depends on the

But, it is cancelled out by the vertical momentum transport.

#### 3.2.5 Horizontal Momentum Transport from Transient Waves

### 3.3 Wave Interactions with Shear Flow on the Beta-Plane

In this section, I discuss the main result of this chapter – the forced response of the shallow-water equations linearized around a zonally uniform shear flow  $\bar{U}(y)$  and height  $\bar{H}(y)$ . I will show that the form of this forced response matches the results of GCM simulations, and suggest that the equatorial jet is therefore vital in controlling the global temperature structure and circulation pattern.

The background flow  $\bar{U}(y)$  and height  $\bar{H}(y)$  satisfy the second line of Equation 3.10, so are geostrophically balanced with  $\bar{H}_y(y) = -y\bar{U}(y)$ . For our Gaussian jet  $\bar{U}(y) = U_0 e^{-y^2/2}$ , the height perturbation is therefore  $\bar{H}(y) = U_0 e^{-y^2/2}$  ([Hammond and Pierrehumbert, 2018](#)).

For the tests in this chapter, I use a forcing magnitude  $Q_0 = 1$  and equal radiative and dynamical damping rates  $\alpha_{rad} = \alpha_{dyn} = 0.2$  ([Matsuno, 1966](#)). I will show the effect of

### 3.3. Wave Interactions with Shear Flow on the Beta-Plane

---

varying these damping rates in Section X.

The tests in this section will show the effect of a zonal flow with a maximum non-dimensional speed between 0 and 1, as this is the speed required for a significant zonal shift of the forced response, as discussed in Section X.

The value of  $Q_0 = 1$  in the forcing  $Q(y) = Q_0 \sin(x)e^{-y^2/2}$  was chosen to produce a comparable perturbation to that from the imposed equatorial jet, and to be consistent with [Matsuno \(1966\)](#) and [Showman and Polvani \(2011\)](#). Later in Section XX I will use a different (and more realistic) forcing value, to satisfy this condition in a spherical geometry with a different balance between jet velocity and jet height.

Linearised around the background flow  $\bar{U}(y)$  and height  $\bar{H}(y)$ , the shallow-water equations in Section X become:

$$\begin{aligned} \frac{\partial u}{\partial t} + \alpha_{dyn}u + \frac{\partial \bar{U}(y)u}{\partial x} + \left( \frac{\partial \bar{U}(y)}{\partial y} - y \right)v + \frac{\partial h}{\partial x} &= 0 \\ \frac{\partial v}{\partial t} + \alpha_{dyn}v + \frac{\partial \bar{U}(y)v}{\partial x} + yu + \frac{\partial h}{\partial y} &= 0 \\ \frac{\partial \bar{H}'u}{\partial x} + \bar{H}'\frac{\partial v}{\partial y} - y\bar{U}(y)v + \frac{\partial h}{\partial t} + \alpha_{rad}h + \frac{\partial \bar{U}(y)h}{\partial x} &= Q(y) \\ \bar{H}' &= 1 + \bar{H}(y) \end{aligned} \tag{3.15}$$

To consider the free modes of this system, we set  $Q(y) = 0$  and  $\partial/\partial t = -i\omega$ , and write  $u, v, h$  in the form  $A(y)e^{i(k_x x - \omega t)}$ :

### 3.3. Wave Interactions with Shear Flow on the Beta-Plane

---

$$\begin{pmatrix} \alpha_{dyn} + ik_x\bar{U}(y) & \frac{\partial\bar{U}(y)}{\partial y} - y & ik_x \\ y & \alpha_{dyn} + ik_x\bar{U}(y) & \frac{\partial}{\partial y} \\ ik_x\bar{H}' & -y\bar{U}(y) + \bar{H}'\frac{\partial}{\partial y} & \alpha_{rad} + k_x\bar{U}(y) \end{pmatrix} \begin{pmatrix} u \\ v \\ h \end{pmatrix} = i\omega \begin{pmatrix} u \\ v \\ h \end{pmatrix} \quad (3.16)$$

$$\bar{H}' = 1 + \bar{H}(y)$$

To find the stationary response to steady forcing, we set we set  $Q(y) = Q_0 e^{-y^2/2}$  (Mat-suno, 1966) and  $\partial/\partial t = 0$ , giving the linear system of equations:

$$\begin{pmatrix} \alpha_{dyn} + ik_x\bar{U}(y) & \frac{\partial\bar{U}(y)}{\partial y} - y & ik_x \\ y & \alpha_{dyn} + ik_x\bar{U}(y) & \frac{\partial}{\partial y} \\ ik_x\bar{H}' & -y\bar{U}(y) + \bar{H}'\frac{\partial}{\partial y} & \alpha_{rad} + k_x\bar{U}(y) \end{pmatrix} \begin{pmatrix} u \\ v \\ h \end{pmatrix} = \begin{pmatrix} 0 \\ 0 \\ Q(y) \end{pmatrix} \quad (3.17)$$

$$\bar{H}' = 1 + \bar{H}(y)$$

I solved both the free and forced systems of equations using the method in Appendix X, expanding the solutions in terms of the parabolic cylinder functions. This method identifies the exact free and forced solutions in the case where  $\bar{U}(y) = 0$ , and finds the solutions with non-zero  $\bar{U}(y)$  to better than 1 part in 10,000 when 30 basis modes are used in the calculation. In Appendix X, I show the accuracy of this method in more detail.

Finally, it is worth noting that I have considered the perturbations in the forced system to apply to a single shallow-water layer of height  $H_0$ , non-dimensionalised to unity. Technically, the vertically varying heating profile in a planetary atmosphere excites a continuum of vertical modes, each defining a shallow-water system of different  $H_0$ . However, Tsai et al. (2014) showed that in this forced shallow-water system, almost all of the energy is

### 3.3. Wave Interactions with Shear Flow on the Beta-Plane

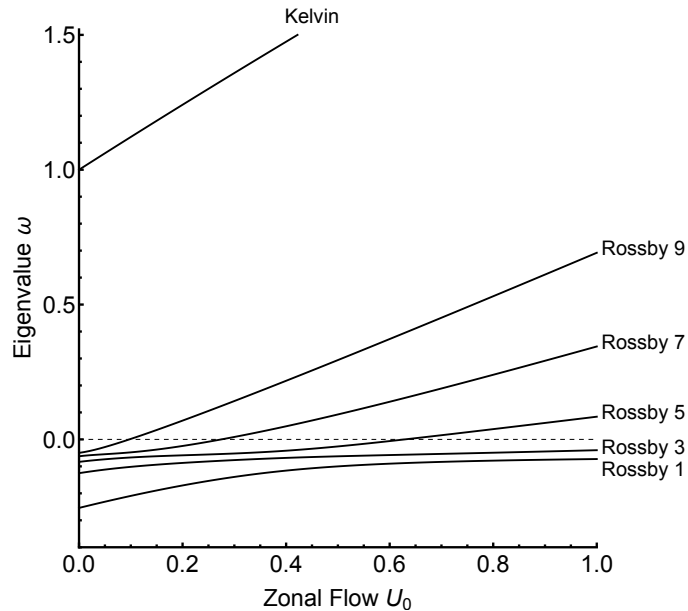


Figure 3.6: Eigenvalue shift.

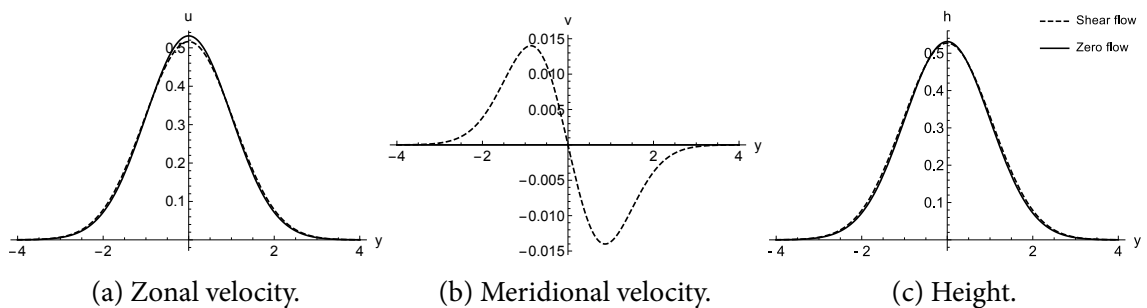


Figure 3.7: The meridional structure of the free Kelvin mode.

confined to the lowest-order vertical mode, making the assumption that a real atmosphere is described well by a single shallow-water layer reasonable.

### 3.3. Wave Interactions with Shear Flow on the Beta-Plane

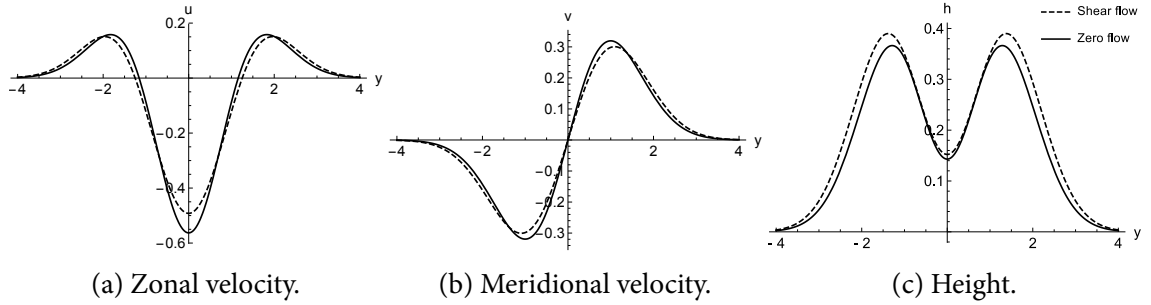


Figure 3.8: The meridional structure of the free Rossby mode ([Hammond and Pierrehumbert, 2018](#)).

#### 3.3.1 Free Modes

In this section, I will discuss the effect of a background shear flow on the free modes of the shallow-water equations. This will be useful to understand the effect of the background flow on the forced response, in the next section.

In Section 3.1, I showed how the response to a forcing can be written as a sum of the free modes of the system. It is not possible to write down an exact solution like this when the system is linearised about a background flow  $\bar{U}(y)$  and  $\bar{H}(y)$ , but it is still useful to interpret the resulting solution in terms of the fundamental free modes.

I will write the free solutions to shallow-water equations as a complex function of latitude  $A(y)$ , and the forced solutions as functions of both latitude and longitude in the form  $A(y)e^{i\delta(y)x}$ . This phase  $\delta(y)$  determines the longitudinal structure of the forced response, and is equivalent to the phase shift  $(\omega_m - k_x \bar{U})$  derived for a uniform flow in Section XX.

We can still consider the response to forcing as a sum of the free modes of the system, as in Section X. Now the equations are linearised about a shear flow  $\bar{U}(y)$  and  $\bar{H}(y)$ , the free modes have a different latitudinal structure  $u(y), v(y), h(y)$  and have different

### 3.3. Wave Interactions with Shear Flow on the Beta-Plane

---

eigenvalues  $\omega_m$  (so will have different longitudinal position in the forced response).

I found the free modes of the shallow-water system defined by Equation 3.16 using the method in Appendix X. Figure 3.6 shows the real parts of the eigenvalues of the free Kelvin mode and the symmetric free Rossby modes of Equation 3.16, for a background flow  $\bar{U}(y) = U_0 e^{-y^2/2}$  with a variable magnitude  $U_0$  ([Hammond and Pierrehumbert, 2018](#)). I plot these modes as they are the lowest-order (so largest magnitude) modes excited by the symmetric, stationary forcing.

The value and sign of these eigenvalues determine the position of the free mode in the forced response, similar to Equation X in Section X. Note that an exact forced solution in terms of a series free modes is now not possible as the flow is not uniform, but it is still very useful to interpret the forced response in this way.

As the magnitude  $U_0$  of the equatorial jet  $\bar{U}(y)$  increases, all of the eigenvalues of the free modes become more positive, corresponding to an eastward shift in their position in the forced response (as in Equation X in Section X). The Kelvin mode already has a positive eigenvalue for  $U_0 = 0$  (hence its position in Figure 3.3a), and this becomes larger as  $U_0$  increases, so the Kelvin mode becomes further east in the forced response. The maximum shift of the modes is to +90° east of the substellar point (as in Equation X), no matter how large the eigenvalue becomes. This shift leads to the large eastward equatorial hot-spot shift that will be seen later.

The Rossby modes are a little more complicated. [Tsai et al. \(2014\)](#) shows that in a uniform background flow, the  $n = 1$  Rossby mode is shifted eastwards towards +90°, producing a hot-spot shift (reproduced in Figure 3.3b). In fact, Figure 3.6 shows that in this non-uniform flow  $\bar{U}(y)$ , the  $n = 1$  Rossby mode eigenvalue becomes less negative but does not

### 3.3. Wave Interactions with Shear Flow on the Beta-Plane

---

become positive for  $U_0 = 1.0$ . This means that in the forced response it is shifted eastwards, but not far enough to pass the substellar point.

The higher order Rossby modes are shifted by the flow  $\bar{U}(y)$ , as shown by their positive eigenvalues for high enough flow speed  $U_0$ . However, the higher the order of a mode, the weaker its contribution to the forced response ([Matsuno, 1966](#)). The  $n = 3$  and  $n = 5$  symmetric Rossby modes are still important to the forced response, but any modes beyond this are less important.

**That is not to say that the  $n = 1$  mode is never responsible for the hot-spot shift – later, we will show that in a spherical geometry the  $n = 1$  mode shifts close to  $+90^\circ$  eastwards. It is also possible in the beta-plane system for different input parameters (flow speed, damping rates) to shift the  $n = 1$  Rossby mode past the substellar point. But, our free mode expansion has shown that the  $n = 1$  Rossby mode is not the only important mode, and that the higher-order modes are also important to the forced response.**

For zero damping, half of these eigenvalues will have positive imaginary parts, and the modes corresponding to them will grow exponentially. Non-zero damping decreases the imaginary part of all the modes, so will make some or all of these modes stable. In general, the free linear system in Equation 3.16 will have some unstable modes unless the damping is very large. These unstable modes are similar to those discussed by ?, who show how similar modes can produce superrotation even on a planet without a permanent day-night heating difference.

These unstable modes technically make the linear forced wave problem ill-posed, since the result of any linear initial value problem will be eventually dominated by the most

### 3.3. Wave Interactions with Shear Flow on the Beta-Plane

---

rapidly growing modes rather than the stationary response. Later comparison with nonlinear GCM simulations in Section ?? will show that the forced response still has considerable explanatory power. This may be because in reality the unstable modes equilibrate due to damping or nonlinear effects, at a sufficiently low amplitude that they take the form of mobile waves propagating across the forced stationary pattern without significantly disrupting its basic structure. Future work should investigate the exact nature of these instabilities, and the effect of damping and shear flow on their growth rates.

The shear flow also affects the latitudinal structure  $A(y)$  of the modes. The lowest-order free solutions of Equation 3.16 (the Kelvin and Rossby modes), plotted in Figure 3.8 and 3.7, resemble the free solutions with zero shear flow ([Matsuno, 1966](#)), with their latitudinal structure slightly changed by a weak shear flow  $\bar{U} = 0.1e^{-y^2/2}$ . The shear flow perturbs the solutions by adding higher order meridional structure. For example, the meridional wind of the Rossby wave in Figure 3.8 resembles the  $n = 1$  parabolic cylinder function added to the  $n = 3$  function (see Figure C.1a in Appendix ??). [Boyd \(1978\)](#) discusses how a shear flow affects the meridional structure of these modes in more detail.

#### 3.3.2 Forced Solutions

Figure X shows the forced solution in shear flow.

#### 3.3.3 Equilibrium Circulation

The equatorial superrotation reaches a steady equilibrium when the zonal acceleration is zero.

### 3.3. Wave Interactions with Shear Flow on the Beta-Plane

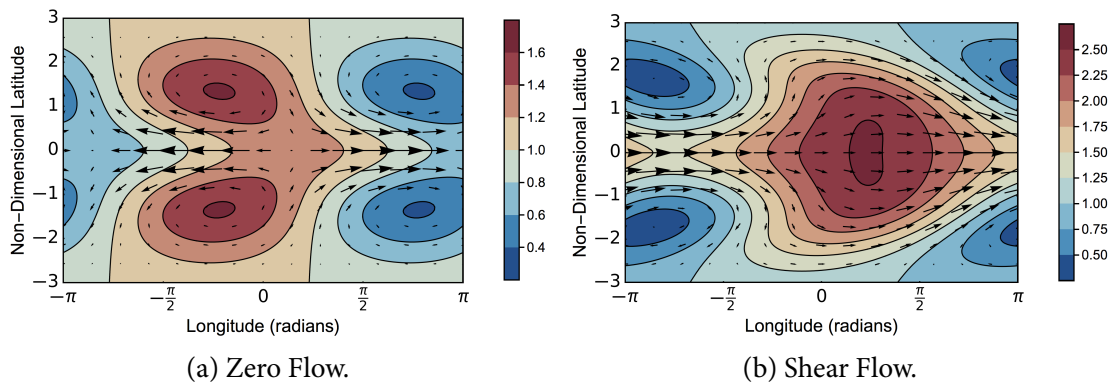


Figure 3.9: Zero Flow and Shear Flow.

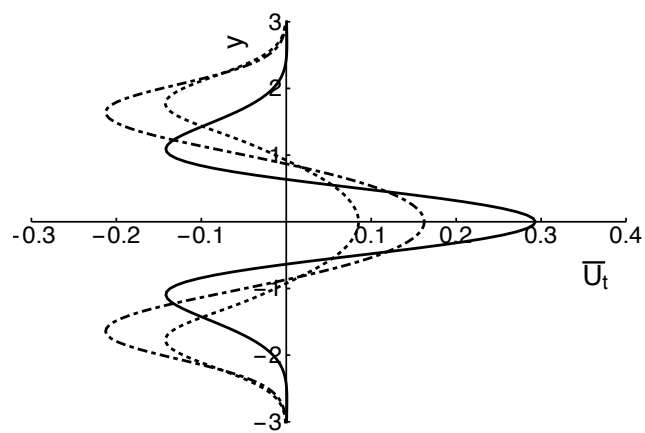


Figure 3.10: Acceleration versus speed

### 3.3. Wave Interactions with Shear Flow on the Beta-Plane

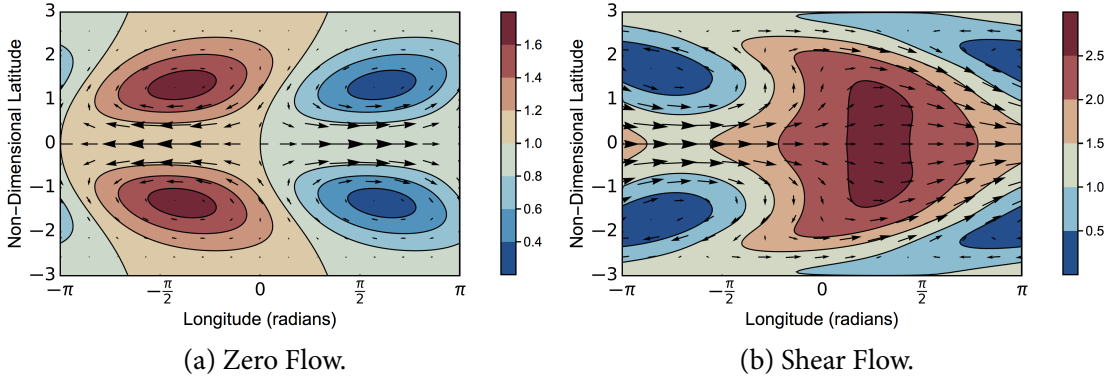


Figure 3.11: Zero Flow and Shear Flow.

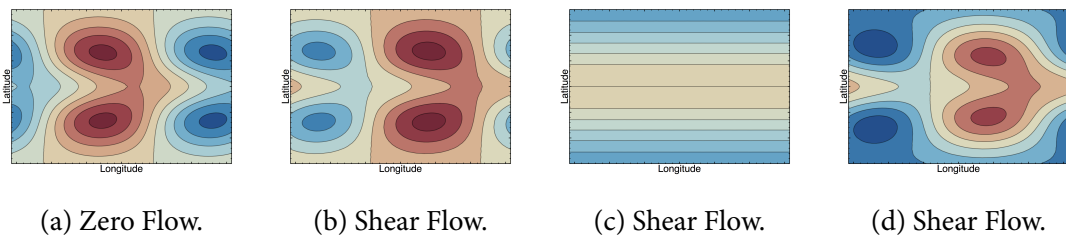


Figure 3.12: Explanation.

As discussed in Section 3.2, the equatorial acceleration decreases as the zonal flow increases, reaching an equilibrium when the acceleration is zero.

#### 3.3.4 Damping

Figure X shows the effect of different damping rates.

### 3.3.5 Hot-Spot Shift

What is the relevance of these forced solutions for the atmospheres of tidally locked planets, and interpreting observations of them?

It is possible to match up the shifted eigenvalues of the free modes in Section X to the total forced response in Section X to understand the change in global temperature structure produced by the equatorial jet.

## 3.4 Wave Interactions with Shear Flow on a Sphere

The beta-plane solutions are intuitive but less accurate for a sphere.

### 3.4.1 Spherical Shallow-Water Equations

### 3.4.2 Forced Solutions

## 3.5 Scaling Relations

### 3.5.1 1D Scaling Relations

### 3.5.2 2D Scaling Relations

## 3.6 Other Jet Patterns

The suite of tests in Chapter XX show that the zonal mean wind profile on a tidally locked planet is not always well represented by a Gaussian. There can be only two jets in

### 3.6. Other Jet Patterns

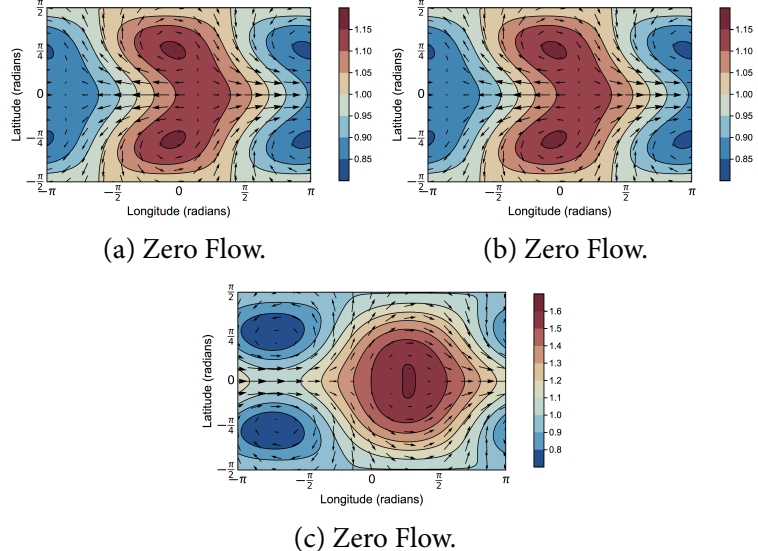


Figure 3.13: Forced linear shallow-water solutions in spherical geometry with and without background shear flows. The parameters of the model are  $\bar{U} = 0.5 \cos \phi \exp(-(\phi/\phi_0)^2)$ ,  $\phi_0 = \pi/3$ ,  $\alpha_{dyn} = \alpha_{rad} = 0.2$ ,  $G = 1$ ,  $Q = 0.5 \cos(\phi)$ , as discussed in Section ??.

the midlatitudes, or three jets, one on the equator.

In this section I find the forced response with different jet profiles, and show that the result is not particularly different to the Gaussian jet used up to this point.

Two Jets:

Three Jets:

One Prograde, Two Retrograde:

One Retrograde, two prograde (eddy-driven):

## CHAPTER 4

# *Equilibrium Circulation States on Tidally Locked Planets*

---

*“Very strange,” he said. “A permanent anticyclone, and inside a huge, calm land that never sees a storm and never has a drop of rain.”*

*“Good place for a holiday then!”*

— Terry Pratchett, *The Last Continent*

Tidally locked planetary atmospheres

### **4.1 Equilibrium Flow Profile**

Chapter X showed that the global circulation and temperature distribution of an atmosphere on a tidally locked planet depends greatly on the zonal jets present on the planet.

**Equatorial Acceleration**

**Midlatitude Acceleration**

**Surface Drag**

**Equatorial Flow Direction**

**Number of Jets**

**GCM Simulations**

Figure X shows a suite of tests (P+H2019) showing how the number of jets varies with rotation rate and temperature.

Figure X shows the spin-up of a very rapidly rotating case.

## 4.2 Initial Conditions

**Starting from Rest**

**Initially Retrograde Flow**

**Initially Strong Prograde Flow**

## 4.3 Instabilities as deviations from equilibrium

**Linear Model Instability Analysis**

The linear model predicts instabilities.

**Instabilities in GCM**

Instabilities appear in the GCM

## 4.4 Jet Scaling Relations

**Equatorial versus Midlatitude Jets**

## CHAPTER 5

# *Non-Linear Tests of a Linear Theory of Tidally Locked Atmospheres*

---

“One might as well approximate the derivatives well instead of badly”

— John P. Boyd, *Chebyshev and Fourier Spectral Methods*

In this chapter, I test the mechanism for the circulation of tidally locked planetary atmospheres predicted in the previous chapter. I use a single-layer non-linear shallow-water model, and a 3D General Circulation Model (GCM) to simulate the atmosphere, and compare the results to the linear theory.

The linear theory simplified the system of a tidally locked planetary atmosphere greatly, and these tests will investigate whether these assumptions were accurate, and test how well the theory predicts the equilibrium circulation.

I will introduce the models used, and show basic tests of whether the mechanism predicted by the linear model is actually at work. I will test the spin-up and equilibrium states of the non-linear models, and compare the results to the scaling relations predicted by the linear model.

This chapter will show that the linear model is a good approximation to the results of the non-linear simulations. The wave-mean flow interaction in the linear theory also applies to the non-linear simulations, suggesting that this is at work on real tidally locked planetary atmospheres as well.

## 5.1 Non-Linear Tests of Linear Shallow-Water Theory

The linear model in Chapter 3 made X main simplifications:

1. The perturbations to the atmosphere are small enough to be approximately linear.
2. The atmospheric response is (on average) stationary, and any transient behaviour does not affect the mean circulation.
3. The atmosphere and the variations in it are small enough in the vertical to be approximated by a shallow model.
4. The day-night forcing is approximated by a relaxation to a constant radiative equilibrium height field.

This section discusses tests of the single-layer linear theory in Chapter 3 using a single-layer non-linear model, which removes the first two assumptions.

### Non-Linear Shallow-Water Model

I used the Geophysical Fluid Dynamics Laboratory Flexible Modelling System (FMS) Spectral Dynamical Core (GFDL-SDC) for non-linear shallow-water simulations. Appendix B describes the model setup.

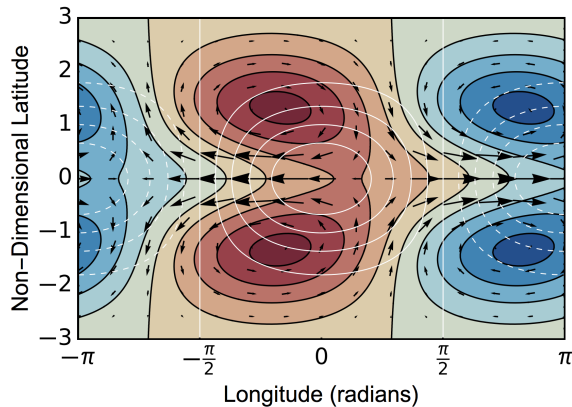


Figure 5.1: The linear response.

## Testing Linearity

The linear model in Chapter 3 is based on a forced linear shallow-water system as discussed in [Matsuno \(1966\)](#). Figure 5.1 shows the response to a forcing  $Q(x, y) = \sin(x)e^{-y^2/2}$  in this linear system.

The linear model assumes that the perturbations in the shallow-water system (representing perturbations in a real three-dimensional atmosphere) are small enough that the linear terms dominate the shallow-water equations. I ran simulations in the non-linear shallow-water model to test whether they matched the linear model at appropriate forcing strength.

The non-linear shallow-water equations are:

The linear solution in spherical coordinates in Figure X in Chapter X has  $\alpha_{rad} = \alpha_{dyn} = 0.2$ ,  $G = 1$  and  $\Delta h/H = 0.5$ . To match this in the non-linear model, I set  $\alpha_{rad} = \alpha_{dyn} = 0.2$ ,  $\Delta h = 5$  km, and  $H = 10$  km. To set  $G = 1$ , I set  $R = R_{Earth}$  and  $g = 10$ , then tuned the rotation rate to  $\Omega = 4.964 \times 10^{-5} = 0.6807\Omega_{Earth}$ .

## 5.1. Non-Linear Tests of Linear Shallow-Water Theory

---

Figure 5.2 shows the equilibrated height and velocity fields for the non-linear model with these parameters, and zero imposed background flow. The non-linear model matches the linear model in Figure X well, with a similar pattern and perturbation size. There is a small day-night asymmetry in the non-linear mode which is not present in the linear model.

The plots in Figure 5.3 show the non-linear response with a smaller height perturbation  $\Delta h = 1$  km, and a larger height perturbation  $\Delta h = 20$  km. Figure 5.3a with the smaller perturbation has a smaller day-night asymmetry than Figure X.b, which is expected as the smaller perturbation should produce a more linear response. Figure 5.3b with the larger perturbation has a larger day-night asymmetry than Figure 5.2, which is expected as the larger perturbation should produce a less linear response. The pattern is also more different from the linear pattern, showing that the linear approximation is less appropriate at the higher forcing amplitude.

This is all as expected, and shows that the forcing amplitudes used in the linear solutions in Chapter X ( $\Delta h/(H\tau_{rad} \sim 0.1)$ ) and the GCM simulations in Chapter X ( $\Delta T/(T \sim 0.1)$ ) are in a regime that is well represented by the linear approximation.

It is possible that the background flow that is imposed in the linear solutions and emerges in the GCM simulations affects the size of the perturbations and moves the system out of the linear regime. I ran the same non-linear shallow-water simulations as Figure X, but imposed the same jet as in the linear solutions to test if the linear and non-linear solutions still matched.

The simulations had the same parameters as in Figure 5.2. The linear model in spherical geometry in Chapter X has a jet with a non-dimensional velocity of

## 5.1. Non-Linear Tests of Linear Shallow-Water Theory

---

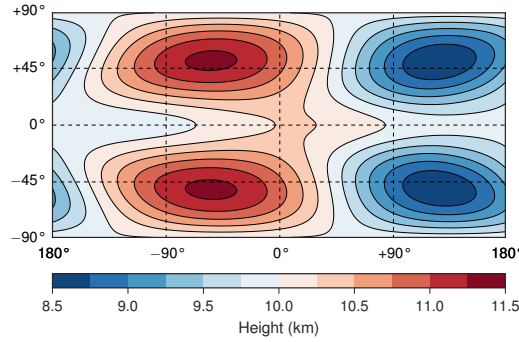


Figure 5.2: 5e3.

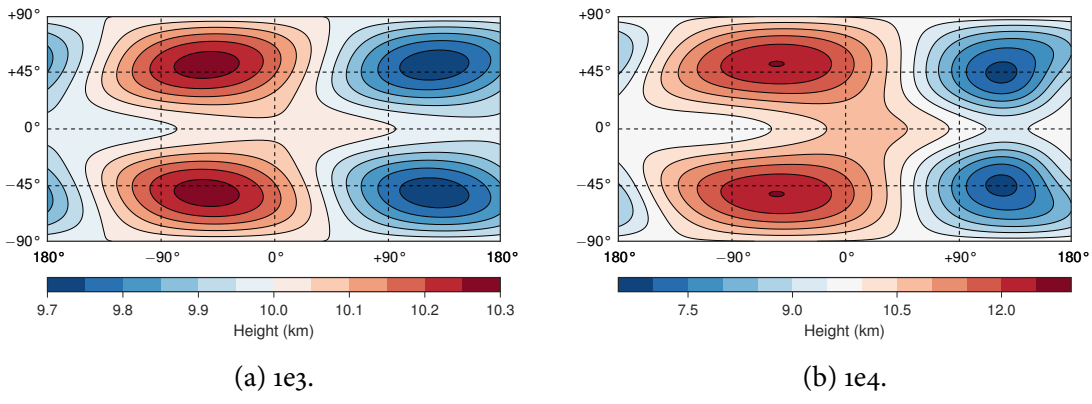


Figure 5.3: Nonlinear.

$0.5 \cos \phi \exp(-(\phi/\phi_o)^2)$ , with a jet width  $\phi_o = \pi/3$ . The non-linear system in Figure 5.2 has a velocity scale of  $R\Omega$ , so I relaxed the non-linear simulations on a timescale  $\tau_{dyn} = 1/\alpha_{dyn}$  to a background flow profile  $R\Omega \cos \phi \exp(-(\phi/\phi_o)^2)$ . Figure 5.4 shows the equilibrated response.

The non-linear response has much less shift at higher latitudes, and a much narrower zonal height field. The zonal flow profile is much narrower than the imposed profile. Figure X shows that subtracting the background flow that is imposed leaves a large retrograde

## 5.1. Non-Linear Tests of Linear Shallow-Water Theory

---

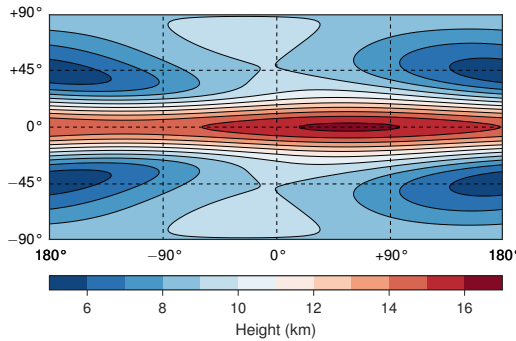


Figure 5.4: Matsuno jet control.

flow in the midlatitudes, as forms in the non-linear Matsuno case. Figure X shows the response and the mean zonal velocity of the case which is not relaxed towards a background flow (the same test as Figure 5.2). This case has westward flow in the midlatitudes, as predicted by Figure X in Chapter X. This mechanism causes the reduced eastward flow in the midlatitudes in the case with a jet in Figure X.

This is responsible for the main difference between the linear and non-linear model. In fact, the acceleration calculated in the linear model does predict this westward midlatitude flow, but it was ignored in Chapter X to match the GCM results.

This highlights a difference between the GCM and the shallow-water models. The shallow-water models always predict a westward acceleration in the mid-latitudes, but this is rarely seen in the GCM. In Chapter X I suggest that eastward acceleration from Rossby wave breaking is responsible for the midlatitude eastward flow in the GCM.

These simulations have shown that the linear model is an appropriate approximation for the atmosphere of a tidally locked planet, but that it does not correctly predict the acceleration away from the equator.

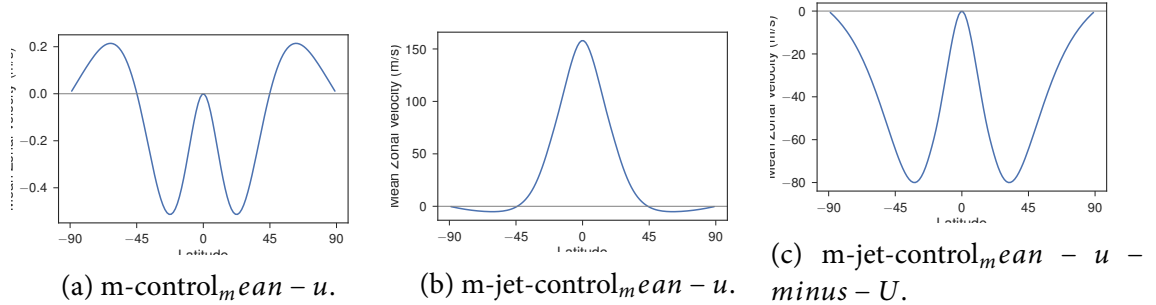


Figure 5.5: Nonlinear with and without imposed jet.

## Testing R Term

[Showman and Polvani \(2010\)](#) shows that the  $R$  term in Chapter X is vital to the equatorial superrotation seen on tidally locked planets.

Figure X shows the height field and mean zonal wind of the non-linear shallow-water model with this  $R$  term added. Similar to Figure X in [Showman and Polvani \(2010\)](#), it shows equatorial superrotation.

It has the same parameters as Figure X but has the  $R$  term added, which is why it has equatorial superrotation but Figure X does not. Section X in Chapter X shows how the  $R$  term produces this effect, as does Figure X in Chapter X.

Like Figure X in [Showman and Polvani \(2010\)](#), there is a retrograde flow in the midlatitudes (where the prograde momentum is transported out of). This retrograde flow is not seen in the GCM, so there must be another effect involving vertical transport of retrograde momentum out of this layer.

Figure X shows tests with different parameters, showing how the equatorial jet speed depends on the parameters. For the default parameters of XX, the equatorial jet is very

---

## 5.1. Non-Linear Tests of Linear Shallow-Water Theory

slow. For the parameters X, the jet speed is comparable to the GCM results in Section X.

### Testing Zonal Flow Profile

The zonal flow profile in Figure 5.5a matches the predicted shallow-water acceleration with R in Chapter X.

ALSO DO TEST WITHOUT R!

### Testing Equilibrium State

Chapter X discusses the jet acceleration.

The time-stepped model reaches an equilibrium state after about X days. The transient response from the impulse generated by turning on the forcing dissipates, and a steady state is reached.

Show wave components, hot-spot, and wind directions.

Figure X shows the equilibrium state for the model with forcing X and rotation rate X.  
Figure X shows the eddy state, showing how the waves have shifted.

### Testing Jet Spin-up

I ran tests to show how the atmosphere reaches this state.

Figure X shows the eddy state over time of the previous test.

Figure X shows the Rossby and Kelvin components over time of the previous test.

Spin-up of height field, eddy height field, and Rossby and Kelvin components.

## Scaling Relation Tests

Test effect of rotation rate, forcing, jet speed.

Figure X shows the equilibrium state for the model with the same forcing X and different rotation rates X.

Figure X shows the equilibrium state for the model with different forcing X.

Figure X shows the equilibrium state for the model with different jet speed X.

## 5.2 GCM Tests of Shallow-Water Theory

I used the GCM Exo-FMS, based on the Geophysical Fluid Dynamics Laboratory Flexible Modelling System (GFDL-FMS). Chapter ?? and Appendix A describe this model.

### Test Planets

In Chapters XX I have treated the atmospheres of terrestrial and gaseous planets similarly.

This is because the shallow-water model only assumes that the atmosphere has a heating profile which excites a wave-1 vertical mode (which should be the case for gaseous planets like XX and terrestrial planets like XX).

I set up two test planets, which I then varied the parameters of.

The terrestrial planet was XX.

The Hot Jupiter was XX.

---

## 5.2. GCM Tests of Shallow-Water Theory

### **Testing Equilibrium State**

Show wave components, hot-spot, and wind directions.

Terrestrial Planet:

Gas Planet:

### **Testing Jet Spin-up**

Spin-up of height field, eddy height field, and Rossby and Kelvin components.

Terrestrial Planet:

Gas Planet:

### **Scaling Relation Tests**

Test effect of rotation rate, forcing, jet speed.

Terrestrial Planet:

Gas Planet:

### **Jet Number and Direction/Circulation Regime**

Terrestrial Planet:

Gas Planet:

## CHAPTER 6

# *Linking the Climate and Thermal Phase Curve of 55 Cancri e*

---

*“One face is forever sunlit, and one forever dark, and only the planet’s slow lib-  
eration gives the twilight zone a semblance of seasons.”*

— Stanley G. Weinbaum, *The Lotus Eaters*

Now that I have introduced lava planets and 55 Cancri e in Chapter 2, laid out a theory of their circulation in Chapters 3 and X, and discussed the numerical model I used to simulate them in Chapter ??, I can move to the central question of this thesis. Namely, how to interpret the thermal emission phase curve of a tidally locked lava planet? The remaining chapters of my thesis will investigate this in increasing detail.

The first phase curve of a Super-Earth was measured by [Demory et al. \(2016\)](#) using Spitzer observations of 55 Cancri e, following the measurement of transits in the visible ([Winn et al., 2011](#)) and infrared ([Demory et al., 2011](#)). This presented the first observation directly linked to the global circulation of a terrestrial planet outside our solar system. It provides an opportunity to test the theories and simulations of the atmospheric circulation

---

of a tidally locked planet that have been shown previously in this thesis.

The thermal phase curve of 55 Cnc e presents the possibility of testing this picture of lava planets, and in particular to determine whether the phase curve demands the presence of a thick noncondensable background atmosphere. In this paper, we use a general circulation model (GCM) to model a range of hypothetical climates for 55 Cnc e and reconstruct their thermal phase curve, in order to test whether the observed phase curve is inconsistent with the presence of a thick atmosphere. We explore which atmospheric compositions are compatible with the phase curve. The results we have obtained for 55 Cnc e will carry over readily to the interpretation of other lava planet phase curves when they become available. The general utility of thermal phase curves in determining characteristics of exoplanets and their atmospheres has been discussed in Selsis et al. (2011) and Maurin et al. (2012).

The analysis in this paper builds on the results of Cowan Agol (2011), Menou (2012), and Komacek Showman (2016), who explored the effect of parameters such as the mean molecular weight on the thermal phase curve of Hot Jupiters via the radiative and advective timescales. Koll Abbot (2015) modelled the relation between atmospheric properties and broadband thermal phase curve for terrestrial planets in a regime (expected to be appropriate to most tidally locked planets) with a significant phase curve amplitude, but very little hot-spot offset. We have identified a regime which can support both a notable amplitude and offset.

Section 2 describes our model and explains the physical processes which it includes. Section 3 lays out the current theory of global circulation on tidally locked planets, where we discuss the key nondimensional parameters and situate 55 Cnc e in the space of circulation regimes. We describe the results from our experiments in Section 4, focusing on

their temperature distributions and simulated phase curves in comparison to the results of Demory et al. (2016b). Further interpretation of the results is provided in Section 5 and our principal findings are summarized in Section 6.

Our best-fit clear-sky atmosphere has a surface pressure of 5 bar and a mean molecular weight of 4.6 gmol<sup>1</sup>. This molecular weight would support the hypothesis of an H<sub>2</sub>-rich atmosphere; however, it is the observed hot-spot phase shift which favours low molecular weight, underscoring the importance of accurate measurements of this quantity for future observations of 55 Cnc e and other lava planets. A diagnostic estimate of cloud effects indicates that Na clouds would not form in such an atmosphere, but that SiO clouds could form on the night-side and bring the modeled night-side brightness temperature more in line with observations. Our results on the vertical structure of the temperature pattern underscore the importance of future measurements of spectrally resolved phase curves for 55 Cnc e and other lava planets, which would provide an important window into atmospheric composition and dynamics.

In the next chapter, I will show how we coupled a more realistic radiative transfer scheme and a dynamic cloud model to Exo-FMS, in order to test the questions raised by this chapter.

## 6.1 Observations of 55 Cancri e

### 55 Cancri e

The first phase curve of a Super-Earth was measured by Demory et al. (2016b) using Spitzer observations of 55 Cancri e, following the measurement of transits in the visible

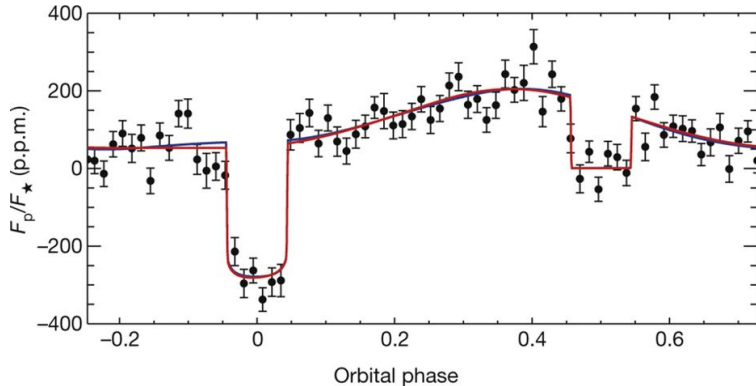


Figure 6.1: Phase curve.

(Winn et al. 2011) and infrared (Demory et al. 2011). 55 Cnc e is a Super-Earth discovered by McArthur et al. (2004) with mass  $8.63 M_{\oplus}$  and radius  $2.00 R_{\oplus}$  in a close, tidally locked orbit with period 0.737 days.

## Thermal Phase Curve

The thermal phase curve has a large amplitude and an offset between its secondary eclipse and its phase maximum. Demory et al. (2016b) used the curve to reconstruct a temperature map with a maximum hemisphere-averaged  $4.5\mu\text{m}$  brightness temperature of  $(2700 \pm 270)$  K, day-night contrast of  $(1300 \pm 670)$  K, and a hot-spot shifted eastwards by  $(41 \pm 12)$ ■

## Possible Atmosphere

55 Cnc e is a member of a class of planets known as “lava planets” which are in such close orbits that they are likely to be tide-locked and have a permanent dayside magma ocean. It

## 6.1. Observations of 55 Cancri e

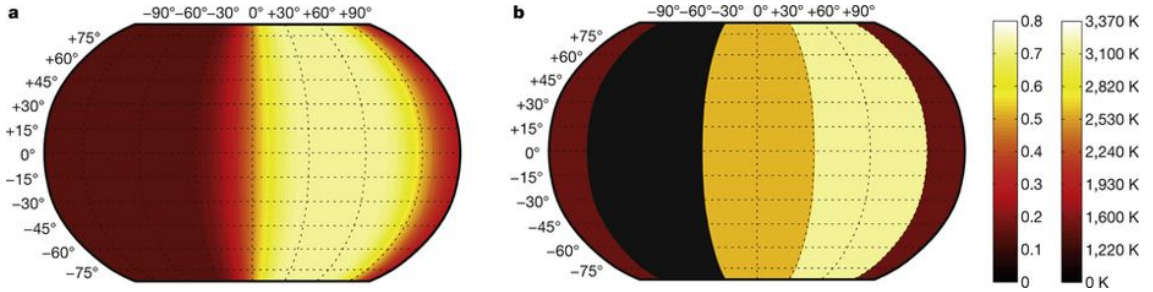


Figure 6.2: Temperature map.

has been argued that the atmospheres of such planets could consist of thin mineralvapour atmospheres outgassed from the magma ocean (L'eger et al. 2011) (Castan Menou 2011). Such thin atmospheres, consisting of a few millibar or less surface pressure, cannot transport much heat apart from possible lateral heat redistribution within the magma ocean, so would yield a phase curve very similar to that of an airless rocky planet with a very cold night-side such as discussed by Maurin et al. (2012).

The transit depth spectra reported in Tsiaras et al. (2016) require a thick H<sub>2</sub>-rich atmosphere. However, Lammer et al. (2013) calculated that an H<sub>2</sub> atmosphere on 55 Cnc e would have a hydrodynamic escape rate of up to  $2.8 \times 10^9$  gs<sup>-1</sup>. This implies that a 10 bar atmosphere would be lost in less than one million years, making it implausible that an H<sub>2</sub>-rich atmosphere could be maintained on this planet. However, the study of exoplanets has yielded up many objects that according to previous conceptions should not exist, so in this paper we will take the idea of an H<sub>2</sub>-rich atmosphere seriously, and ask what features of the phase curve measured by Demory et al. (2016b) are compatible with, or demand, a low molecular weight atmosphere. In order to focus on dynamical behavior in this initial study, we make a number of simplifying assumptions regarding the radiative be-

havior of the atmosphere. First, we assume the atmosphere to be transparent to incoming stellar radiation, so that all of the shortwave radiation is absorbed at the ground, leading to a deep day-side convective layer. This assumption is based on estimates of the shortwave opacity of likely cloud-free atmospheres of up to 10 bars. The addition of a small amount of shortwave opacity would not change our results much, so long as atmospheric absorption occurs near enough the surface to drive a convective troposphere. Very thick shortwave-opaque atmospheres could instead have a deep radiative-equilibrium layer with a thin dynamically active layer near the top; we shall not consider such atmospheres in the present paper. In the infrared, the atmosphere is assumed to act as a grey gas with specified optical thickness and opacity. This is not inconsistent with the assumption of an atmosphere largely transparent to incoming stellar radiation, because 55 Cancri is a G star, with a relatively low proportion of its output in the near-IR. The use of gray gas radiation for climate calculations is not a serious source of inaccuracy as the circulation is primarily affected by the radiation scheme via the surface temperature relative to the radiating temperature of the planet. The optical thickness can be tuned to match the temperature that would be yielded by an assumed real-gas atmosphere, so in this paper we use primarily as a way to control surface temperature. Non-grey radiative effects are taken into account when we interpret the results in terms of the corresponding Spitzer  $4.5\mu\text{m}$  phase curve, in that we consider the emission from a range of different atmospheric levels and not just the grey radiating level. This allows for the possibility that the atmospheric composition may support an infrared window region near  $4.5\mu\text{m}$ , allowing radiation from deeper in the atmosphere, or a source of anomalous opacity (e.g. clouds) there, forcing the radiating level to be higher in the atmosphere. The surface pressure determines the atmospheric mass

via the hydrostatic relation. For a given surface pressure and , atmospheric composition affects the climate through mean molecular weight and specific heat. However, molar specific heat is only weakly dependent Climate of 55 Cancri e 3 on composition, because it is primarily determined by the number of active degrees of freedom. For example, at 2000K the molar specific heats of CO, N<sub>2</sub> and H<sub>2</sub> vary by no more than 3.435.5 Jmol<sup>-1</sup>K<sup>-1</sup>, with similar results for other common diatomic gases. Triatomic gases have only a modestly greater molar specific heat at 2000K, e.g. 6% for CO<sub>2</sub> or 4% atmosphere's ability to transport heat, is mostly determined by surface pressure and molecular weight. The mean molecular weight also affects the speed of gravity waves in the atmosphere, through its influence on the gas constant. This speed determines the character of many atmospheric waves which directly transport heat and are implicated in the generation of super-rotating low-latitude jets, which also transport heat. We present our simulation results in terms of a range of H<sub>2</sub>-N<sub>2</sub> mixtures, but they would apply accurately to any other diatomic mixture with the same molecular weight, and with only moderate inaccuracy to triatomic-dominated mixtures.

## Atmospheric Circulation

The measured phase curve of 55 Cnc e exhibits two features that demand substantial horizontal heat transport. First, the hot spot of the planet is shifted 41° eastward relative to the substellar point. Second, the nightside temperature of the planet is quite high – on the order of 1300K – demanding delivery of  $1.6 \times 10^5 \text{ W/m}^2$  of heating to maintain it. However, the day-night temperature difference is also large – on the order of 1300K – which puts a limit on the efficiency of the heat transporting mechanism. It has been sug-

gested that the implied heat transport on 55 Cnc e might be carried by the magma ocean. However, Kite et al. (2016) argued that a magma ocean could not redistribute enough heat to affect a planet’s measured phase curve. It is also conceivable that tidal heating could contribute to maintaining the night-side temperature. In this paper, we will focus on the question of whether atmospheric heat transport alone can account for the phase curve, though we will offer some remarks in Section 5 on problems with tidal heating as an explanation of the night-side temperature. The hot-spot phase shift and phase curve amplitude on tide-locked planets have been extensively studied in connection with interpretation of Hot Jupiter phase curves. For sufficiently short period orbits, the global circulation of such atmospheres is dominated by the effects of planetary scale equatorial Rossby and Kelvin waves which drive a superrotating jet (Showman Polvani (2011), Heng Showman (2015)). The circulation system transports heat eastwards around the equator, shifting the hot-spot from the substellar point and warming the night-side of the planet. The observed phase curve of 55 Cnc e poses the particular challenge that its large 41 $\pm$  hot-spot shift suggests strong heat redistribution, but its large 1300 K day-night difference suggests weak heat redistribution. The need to negotiate the tension between these two requirements puts strong constraints on the kind of atmosphere the planet can have.

## 6.2 Simulating a Lava Planet

We modelled the atmosphere of 55 Cnc e using Exo-FMS, an idealised general circulation model (GCM) based on the finite-volume dynamical core of the software framework FMS described by ?. Other GCMs using the FMS framework have been used to model ter-

restrial, tidally locked exoplanets by ?, ?, ?, and ?. Other GCMs have been used to model tidally locked super-Earths by ?, ?, and ?. Our model planet has radius  $r_p = 1.91 r$ , orbital period  $P = 0.737$  days, surface gravity  $g = 21.7 \text{ ms}^{-2}$  (?), and incoming stellar flux  $3.55 \times 10^6 \text{ Wm}^{-2}$  (?).

Our model is the same as that used in ?, but with a dry atmosphere (no condensable species). It uses the 3D fluid-dynamical core on a  $144 \times 96 \times 40$  grid, a 1D grey-gas radiative solver, and a 1D dry-convective adjustment routine. The top pressure level is  $10^{-5} p_s$ , for surface pressure  $p_s$ . The model solves the primitive equations, then calculates the radiative fluxes and heating in each 1D column of the grid and updates their temperature, then adjusts any unstable parts of each column towards the dry adiabat. We use two-stream grey-gas radiative transfer so as to focus on key dynamical aspects of the problem. At temperatures as high as that of 55 Cnc e, a small portion of the emitted radiation has short enough wavelength that it can be affected by Rayleigh scattering, but we neglect this effect.

The specific calculations reported here are for atmospheres with the thermodynamic properties of H<sub>2</sub>-N<sub>2</sub> mixtures, though as noted in the introduction the composition affects the thermodynamic properties primarily through the mean molecular weight of the mixture. The actual composition has a much stronger effect on the radiative properties of the atmosphere, captured in our simulations by the specified infrared optical thickness  $\tau_\infty$ . To provide a point of reference, we carried out 1D radiative-convective simulations for 55 Cnc e for a 10 bar pure H<sub>2</sub> atmosphere, using both a realistic representation of the H<sub>2</sub> collisional opacity (based on (?)) and a grey-gas approximation. It was found that the surface temperature and vertical structure were nearly identical between the real-gas calculation and a grey-gas calculation with grey optical depth  $\tau_\infty = 8$ , so the surface temperature we

quote for this case can be considered realistic for a pure 10 bar H<sub>2</sub> atmosphere. This corresponds to an opacity of 22.4 cm<sup>2</sup>kg<sup>-1</sup>, which we used in all of our tests (apart from those in Section 6.4.3) in order to compare the effect of other parameters. In reality,  $\kappa$  should scale quadratically with pressure if it were only due to collision-induced absorption. Given the range of possible constituents that could contribute to the infrared opacity of the atmosphere, we treat  $\tau_\infty$  as an independent parameter of the atmosphere; this helps to isolate the dynamical vs. radiative effects of composition.

In the model, the outgoing 4.5  $\mu$ m radiation is radiated from the upper reaches of the atmosphere in all our tests, as they all have a high grey-gas optical thickness. In reality, the real-gas absorption spectrum might have a stronger or weaker opacity at 4.5  $\mu$ m than the assumed “average” of the grey-gas approximation. This means that 4.5  $\mu$ m radiating level relevant to the Spitzer observations of ? could be higher or lower in the atmosphere than in our results, so we will consider the temperature distribution at multiple levels of the atmosphere and not just at the grey-gas radiating level.

We neglected atmospheric absorption of incoming stellar flux, as our 1D real-gas radiative-convective model showed that the H<sub>2</sub> shortwave absorption is too weak to greatly affect the temperature profiles (and N<sub>2</sub> shortwave absorption is even weaker). Given high infrared opacity, introduction of a moderate shortwave opacity would not significantly change our results, as only a small amount of shortwave radiation needs to reach the surface in order to maintain a deep convective troposphere, as is exemplified by the case of Venus (?), Ch. 4). Introduction of a very strong upper-atmosphere shortwave absorber, such as could be caused by some types of clouds, would fundamentally alter the picture by creating a deep non-convective isothermal layer extending from the surface to the absorb-

ing layer. We do not consider such situations in this paper, but the possibility needs to be kept in mind.

We set the surface albedo to zero and neglected the scattering albedo of the atmosphere. This means that any temperatures from our results are an upper bound, as the absorbed stellar flux will be lower. However, a low albedo seems likely for the planet given the observed high brightness temperature.

The models were initialised with zero wind speed and the same temperature profile in each vertical column, which had a specified surface temperature and followed the dry adiabat up to a certain temperature, where it was set to an isotherm. ? showed that the results of models of tidally locked Hot Jupiter atmospheres are insensitive to initial conditions, so we do not expect our results to be sensitive to this choice of initialisation.

Following ? we regarded the circulation to have reached equilibrium when the top of atmosphere radiation budget is in balance and the stratospheric temperature stops evolving. We also checked that the global mean temperature and the winds had stopped evolving. In contrast to the 300 days it typically took the simulations of the tidally locked planet Proxima b in ? to equilibrate, our simulations had generally reached equilibrium after 10 Earth days, owing to the short radiative time scale associated with the high temperature of a lava planet. All results presented are for averages over the final 10 days of 50 day runs.

## 6.3 Simplified Scaling Theory

We will now discuss the characteristic time and length scales, and corresponding nondimensional parameters, that govern a planet's heat-transport properties. The funda-

### 6.3. Simplified Scaling Theory

---

mental externally imposed velocity scale is the external gravity wave speed  $U_{wave} = \sqrt{\frac{R^* T}{\mu}}$ , where  $\mu$  is the mean molecular weight of the atmosphere,  $R^*$  is the universal gas constant, and  $T$  is the characteristic temperature of the dynamically active layer of the atmosphere, assumed here to be on the same order as the mean radiating temperature of the planet. ? use a somewhat different expression to estimate  $U_{wave}$ , but the result differs only by order an order unity constant from the one used here.

From  $U_{wave}$  we can build the global radius of deformation

$$L_d \equiv \frac{\sqrt{R^* T / \mu}}{\Omega} \quad (6.1)$$

and the wave timescale

$$t_{wave} \equiv \frac{r_p}{U_{wave}} = r_p \sqrt{\frac{\mu}{R^* T}} \quad (6.2)$$

where  $\Omega$  is the angular velocity of the planet's spin ( $2\pi/P$  for the tide locked case). A key nondimensional parameter governing the dynamical regime is then

$$\Lambda \equiv \frac{L_d}{r_p} = \frac{1}{\Omega t_{wave}} \quad (6.3)$$

$\Lambda$  is the Weak Temperature Gradient (WTG) parameter discussed in ?, and constitutes a nondimensional measure of the importance of the planet's rotation. Large  $\Lambda$  corresponds to a slowly rotating planet, in which the Coriolis force is too weak to support large temperature gradients. Such planets (with some caveats, discussed in ?) tend to have globally weak horizontal temperature gradients. Planets with  $\Lambda$  order unity or smaller are more Earthlike, with strong meridional (north-south) temperature gradients and strong zonal (east-west) jets. Such planets can still have small zonal temperature gradients owing to

### 6.3. Simplified Scaling Theory

heat transport by the jets, but the magnitude and phase shift of such variations depends on the magnitude of radiative damping.

For 55 Cnc e, using a typical temperature of 2500K,  $\Lambda$  ranges from 2.7 for a pure H<sub>2</sub> atmosphere to 0.72 for a pure N<sub>2</sub> atmosphere. To put these values into perspective,  $\Lambda = 0.6$  for Earth, which exhibits strong midlatitude temperature gradients but weak tropical temperature gradients, though it should be kept in mind that tide-locked planets have a stronger zonal variation in stellar heating than does Earth. Hot Jupiters have a similar  $L_d$  to 55 Cnc e, but much larger radius, and therefore have much smaller  $\Lambda$  and are correspondingly more strongly influenced by rotation. Very low molecular weight atmospheres on 55 Cnc e edge more into the WTG regime, with the dynamical effects of rotation becoming more dominant as molecular weight is increased, but any atmosphere the planet might have will put it in a dynamical regime that is strongly influenced by rotation.

One can also define a time scale based on the characteristic jet speed  $U$  on the planet

$$t_{adv} \equiv \frac{r_p}{U} \quad (6.4)$$

$U$  is not an externally imposed parameter, because it is an emergent property determined by the externally imposed planetary parameters (instellation, atmospheric composition, size, etc.). For rapidly rotating tide-locked planets, the jets primarily take the form of equatorial super-rotating (eastward) circulations. Because of the difficulty of estimating the jet speed *a priori* in terms of the planetary parameters,  $U$  is sometimes chosen based on general circulation model simulations, in which case scalings based on  $t_{adv}$  become diagnostic rather than predictive. Alternatively, insofar as phase curve properties can be shown to depend on  $t_{adv}$ , fits of theoretical to observed phase curves can be used to es-

### 6.3. Simplified Scaling Theory

---

timate the jet speed. ? suggest the equilibrium cyclostrophic wind as a reasonable rough estimate of jet speed; it can be shown that this estimate has the same order of magnitude as  $U_{wave}$ .

Most studies of the phase curve properties have focused on the radiative damping time scale,  $t_{rad}$  relative to  $t_{adv}$  or  $t_{wave}$  as the key nondimensional parameter. For a planet with a deep convective troposphere heated by stellar absorption near the surface,

$$t_{rad} \approx \frac{p_s}{\mu g} \frac{c_{p,mol}}{4\sigma T_{rad}^3} \quad (6.5)$$

where  $p_s$  is the surface pressure and  $c_{p,mol}$  is the molar specific heat.  $T_{rad}$  is the mean radiating temperature of the planet, which is fixed by the planet's net absorption of stellar energy and does not depend on the atmospheric opacity or optical thickness. The pressure used in this expression differs from that in the estimate in ? because we consider planets with a deep convective troposphere, as opposed to fluid planets like hot Jupiters or GJ1214b where the thermal emission almost inevitably comes from a limited radiative-equilibrium layer near the top of the atmosphere. For a given planet,  $t_{rad}$  varies linearly in proportion to  $p_s/\mu$ , so that increasing surface pressure increases the damping time in the same way as decreasing mean molecular weight.  $t_{rad}/t_{wave}$  provides the fundamental a priori measure of the ability of an atmosphere to transport enough heat to even out the day-night temperature difference, though in some cases the diagnostic quantity  $t_{rad}/t_{adv}$  could prove more accurate, in circumstances when  $t_{adv}$  is significantly shorter than  $t_{wave}$ . Letting the transport time  $t_{trans}$  be the lesser of  $t_{adv}$  and  $t_{wave}$ , if they differ significantly, we can identify three regimes:

1.  $t_{trans} \gg t_{rad}$ , where air cools faster than it travels, leading to a strong day-night

### 6.3. Simplified Scaling Theory

---

contrast and a weak hot-spot shift, i.e. a phase curve with a large amplitude and small offset.

2.  $t_{trans} \ll t_{rad}$ , where air travels faster than it cools, leading to a weak day-night contrast and a large hot-spot shift, i.e. a phase curve with a small amplitude and large offset.
3.  $t_{trans} \sim t_{rad}$ , where air cools on the same timescale as it circulates. This may lead to both a significant hot-spot shift and day-night contrast, i.e. a phase curve with a large amplitude and peak offset like the curve of 55 Cnc e.

? modelled cool tidally locked planets and reported that the phase curve amplitude (i.e. the day-night contrast) depends mainly on the ratio of advective to radiative timescales, along the lines sketched out above. ? introduced a more general quantitative estimate of the day-night contrast which takes Coriolis effects into account. It is based on simplified solutions of the primitive equations from ?. In the regime where surface friction is not the controlling factor and the Coriolis effects are comparable to or dominate advection effects, their result reads

$$\frac{\Delta T}{\Delta T_{eq}} \sim 1 - 1/(1 + \frac{t_{wave}^2 \Omega}{t_{rad} \Delta \ln p}) \quad (6.6)$$

where  $\Delta T_{eq}$  is the radiative-equilibrium day-night contrast (i.e. without any convection or bulk dynamics), and  $\Delta \ln p$  is the difference in log pressure between the surface and the relevant pressure level (see ? for details).

Eq. 6.6 can be recast in the form

$$\frac{\Delta T}{\Delta T_{eq}} \sim 1 - 1/(1 + \Lambda^{-1} \frac{t_{wave}}{t_{rad} \Delta \ln p}) \quad (6.7)$$

### 6.3. Simplified Scaling Theory

---

which highlights the influence of the WTG parameter  $\Lambda$ . One can make the day-night temperature contrast weak either by making the WTG parameter large or the nondimensional radiative damping time large.

To estimate the hot spot shift, ? (see their Eq. 47) introduce a kinematic theory balancing radiative damping against advection by a specified jet speed  $U$ . The hot spot shift is a monotonically increasing function of  $t_{rad}/t_{adv}$ , with the hotspot located at the substellar point for  $t_{rad}/t_{adv} \ll 1$  and moving to the terminator as  $t_{rad}/t_{adv} \rightarrow \infty$ .

The atmospheric circulation determining the hot-spot shift and phase curve amplitude is governed by  $\Lambda$  and the nondimensional radiative damping time (e.g.  $t_{rad}/t_{wave}$ ). the latter depends on surface pressure in the combination  $p_s/\mu$  whereas the former depends on  $\mu$  alone. It is this property that opens the possibility of estimating both  $p_s$  and  $\mu$  through interpretation of the observed phase curve. The results quoted from ? suggest that the hot-spot phase shift depends on the nondimensional  $t_{rad}$  alone, whereas the phase curve amplitude depends on  $\Lambda$  as well.

Figure 6.3 shows the parameter space we are investigating, and the regimes with significant hot-spot shift or day-night contrast, calculated using equation 6.6 and Eq. 47 of ?. According to these formulae the area to the right of the blue line has a significant day-night contrast (80% of the equilibrium value with no heat transport), while the area to the left of the red line has a significant ( $>20$ ) hot-spot shift. An atmosphere in the green area between these lines has the best chance to replicate the observed phase curve. The regime boundaries shown in the figure serve only to help situate our simulations in parameter space; our interpretation of the observed phase curve is based on GCM simulations, which depend on the same fundamental nondimensional parameters but take into account numerous phys-

ical effects, such as changes in jet width and strength, not captured by the simple scaling laws.

The infrared optical thickness  $\tau_\infty$  is a third nondimensional parameter of the climate. In the configuration we model, it is of secondary importance so far as the character of the circulation is concerned, since in a mostly convective atmosphere it only sets the surface temperature relative to the radiating temperature. Increasing  $\tau_\infty$  somewhat increases the wave speed through increasing the temperature, but not significantly so over the range of  $\tau_\infty$  we consider. In the case where the atmosphere has a window region near the wavelength at which observations are taken, however, so that the observed brightness temperature reflects temperatures deeper in the atmosphere than the grey-gas radiating level, increasing  $\tau_\infty$  will significantly increase the amplitude of the phase curve.

## 6.4 Results

cccccc 1 Exo-FMS Test Parameters. The first three tests are intended to show the different regimes discussed in section ??, and Test 5 is the “best-fit” composition discussed in section 6.4.2. Note that the molar heat capacity of H<sub>2</sub> and N<sub>2</sub> is almost the same. The opacity  $\kappa$  has been calculated from the chosen  $\tau_\infty$ . The 10 bar H<sub>2</sub> opacity is consistent with the CIA-only results of ?. Test p<sub>s</sub>  $\mu$   $\tau_\infty$   $\kappa$

(bar) (gmol<sup>-1</sup>) (cm<sup>2</sup>kg<sup>-1</sup>) 1 – H<sub>2</sub> 10 2.0 8.0 22.4

2 – N<sub>2</sub> 10 28.0 8.0 22.4

3 – H<sub>2</sub>+N<sub>2</sub> 10 4.6 8.0 22.4

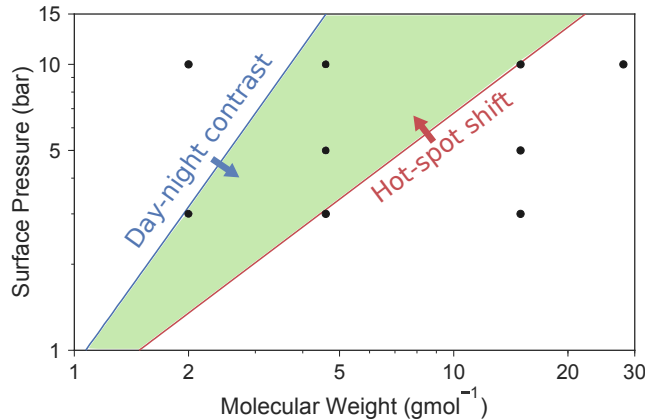


Figure 6.3: Our parameter space, where the green region is the regime predicted to support both a significant hot-spot shift and day-night contrast. The black points show the atmospheres we tested, detailed in Table 6.4. We used a fixed advection speed  $1000 \text{ ms}^{-1}$  and fixed mean temperature  $2000\text{K}$ . The lines correspond to a predicted hot-spot shift of 20 and a day-night contrast of 80% of the equilibrium contrast (with no heat transport). We tested some of the points with multiple values of  $\tau_\infty$  – in our parameter space, we do not expect it to affect the hot-spot shift or fractional day-night contrast (see Sections ?? and 6.4.3).

4 – H<sub>2</sub>+N<sub>2</sub> 5 4.6 4.0 22.4

5 – H<sub>2</sub>+N<sub>2</sub> 3 4.6 2.4 22.4

6 – H<sub>2</sub>+N<sub>2</sub> 10 15.0 8.0 22.4

7 – H<sub>2</sub>+N<sub>2</sub> 5 15.0 4.0 22.4

8 – H<sub>2</sub>+N<sub>2</sub> 3 15.0 2.4 22.4

9 – H<sub>2</sub>+N<sub>2</sub> 5 4.6 2.0 11.2

10 – H<sub>2</sub>+N<sub>2</sub> 5 4.6 8.0 44.8

## 6.4. Results

---

This section shows the results of our tests in Exo-FMS. We modelled ten different atmospheres and compared their phase curves and temperature distributions to those measured and reconstructed by ?. Sections 6.4.1, 6.4.2, and 6.4.3 investigate the effects of mean molecular weight  $\mu$ , surface pressure  $p_s$ , and optical thickness  $\tau_{inf}$ . We focus on the hot-spot shift and day-night contrast of the temperature distributions, which correspond to the offset and amplitude of the phase curves. We then discuss which atmospheres are consistent with the observed phase curve, and how real-gas radiative transfer and cloud formation could fully explain the observations.

cccc 2 Exo-FMS Results Summary. Hot-spot shift and day-night contrast are taken from the half-surface-pressure level, which does not display the largest shift and contrast but is useful for comparison. The day-night contrast is the difference between the warmest and coldest hemispheres, for consistency with ?. These results are a summary of the broad features of each test, and Section ?? discusses these features and the reconstructed phase curves in much greater detail. Test  $p_s$   $\mu$  Hot-spot Day-night  
(bar) (gmol<sup>-1</sup>) (K) Observations +( $41 \pm 12$ ) ( $1300 \pm 670$ )

1 - H<sub>2</sub> 10 2.0 +45 100

2 - N<sub>2</sub> 10 28.0 0 750

3 - H<sub>2</sub>+N<sub>2</sub> 10 4.6 +30 200

4 - H<sub>2</sub>+N<sub>2</sub> 5 4.6 +25 250

5 - H<sub>2</sub>+N<sub>2</sub> 3 4.6 +15 300

## 6.4. Results

---

$H_{210\text{bar}, \text{surf}} p.e^{pso.3} H_2, 10\text{bar}$ : surface air temperature  
 $H_{210\text{bar}, \text{half}} p.e^{pso.3} H_2, 10\text{bar}$ : half-surface-pressure air temperature  
 $10\text{sh}_{\text{half}} p.e^{pso.3} H_2 + N_2, 4.6 \text{ gmol}^{-1}, 10 \text{ bar}$ : brightness temperature

Figure 6.4: 10-day average temperature maps centred on the substellar point, after each Exo-FMS test reaches top-of-atmosphere radiative balance. The first column is surface air temperature, which generally shows the largest day-night contrast as it is strongly coupled to the surface temperature and incoming stellar flux. The second column is the half-pressure air temperature, which generally shows the largest hot-spot shift as it is normally close to the height of the superrotating jet. The third column is the brightness temperature, which determines the thermal phase curve for the model grey-gas radiation – in reality, the thermal emission could be from a different level of the atmosphere.

6 –  $H_2+N_2$  10 15.0 o 150

7 –  $H_2+N_2$  5 15.0 o 550

8 –  $H_2+N_2$  3 15.0 o 600

9 –  $H_2+N_2$  5 4.6 +20 200

10 –  $H_2+N_2$  5 4.6 +25 250

### 6.4.1 Effect of Mean Molecular Weight

We use a pure  $H_2$  atmosphere as a starting point, as the measurements of ? suggested that the atmosphere is  $H_2$ -rich.

Test 1 is a pure  $H_2$  atmosphere, with surface pressure  $p_s = 10$  bar and optical thickness  $\tau_\infty = 8.0$ ; for this case, the surface temperature and vertical structure of the atmosphere are

## 6.4. Results

---

very similar to results that would be obtained with a real-gas radiative transfer calculation taking into account the collisional opacity of H<sub>2</sub>. The theory in Section ?? predicts that this test will have a large hot-spot shift but small day-night contrast, because its radiative timescale is much longer than its transport timescale. The results confirm this, showing a weak day-night temperature gradient but significant hot-spot shift at both the surface and mid-atmosphere levels, though with a more pronounced shift at mid-atmosphere than at the surface. The vertical structure of the temperature pattern will be discussed in Section 6.4.4. The grey brightness temperature  $T_b$  shown in the third column provides a direct indication of the net horizontal heat transport, as the infrared cooling to space is  $\sigma T_b^4$ . Very weak heat transport would manifest as a close resemblance of  $\sigma T_b^4$  to the instellation pattern, whereas complete horizontal temperature homogenization manifests as a uniform  $T_b$ . The latter is very nearly the case for this atmosphere, to the extent that the variations in  $T_b$  are so small that a statistically stationary pattern has not yet fully emerged. In any case, the temperature is too uniform at all levels to be compatible with the observed phase curve. Low molecular weight atmospheres strongly favour weak temperature gradients because the WTG parameter  $\Lambda$  and the radiative damping time  $t_{rad}$  both become larger as molecular weight is decreased.

Test 2 is a pure N<sub>2</sub> atmosphere, with surface pressure  $p_s = 10$  bar and optical thickness held fixed at  $\tau_\infty = 8.0$ . This tested the effect of changing the molecular weight of the atmosphere. Section ?? predicts that N<sub>2</sub> atmosphere will have a large day-night contrast but a small hot-spot shift, as its radiative timescale is much shorter than its transport timescale, and the WTG parameter is also smaller. The results confirm this, as the day-night temperature gradient is large but the hot-spot shift is very small at all levels. Section ?? shows how

this results in a phase curve with a large amplitude but little to no peak offset. The comparison of Test 1 to Test 2 is consistent with the simulations of ?? showing that low molecular weight favours an increased phase shift.

We used these results and the theory in Section ?? to select a composition which might match the observations. Figure 6.3 shows the predicted regimes in our parameter space. The shaded area is the region which should support both a hot-spot shift and day-night contrast. Our first test in this region was Test 3 – an H<sub>2</sub>-N<sub>2</sub> mixture, with mean molecular weight 4.6 gmol<sup>-1</sup>, surface pressure  $p_s = 10$  bar and optical thickness  $\tau_\infty = 8.0$ . Section ?? predicts that this composition could support a large hot-spot shift and a large day-night contrast. Figure 6.4 and Table 6.4 show that both the brightness temperature and the temperature at the half-pressure level have a large hot-spot and day-night contrast, although not as large as the observations. In the rest of this paper, we investigate the effect of surface pressure and optical thickness on the temperature distribution and thermal phase curve, to test our expectations in Section ?? and to find an atmospheric composition which better matches the observations.

In summary, Tests 1, 2 and 3 do not match the measured temperature distribution, but do confirm the general effects of changing the atmospheric properties described in section ???. Table 6.4 lists the test cases and their parameters, and Table 6.4 summarises the results.

### 6.4.2 Effect of Surface Pressure

In this section we discuss a number of simulations with surface pressures of 3, 5, and 10 bar. The tests either have mean molecular weight  $\mu = 4.6$  gmol<sup>-1</sup> or 15 gmol<sup>-1</sup>, corre-

## 6.4. Results

---

$H_2N_2_{10}half\ p.epso.34.6\ gmol^{-1}$ ,  $H_2+N_2$ , 10 bar: half-surface-pressure air temperature  
 $H_2N_2_{5h}half\ p.epso.34.6\ gmol^{-1}$ ,  $H_2+N_2$ , 5 bar: half-surface-pressure air temperature  
 $H_2N_2_{3h}half\ p.epso.34.6\ gmol^{-1}$ ,  $H_2+N_2$ , 3 bar: half-surface-pressure air temperature  
 $15GMOL_{10}half\ p.epso.315\ gmol^{-1}$ ,  $H_2+N_2$ , 10 bar: half-surface-pressure air temperature  
 $15GMOL_{5h}half\ p.epso.315\ gmol^{-1}$ ,  $H_2+N_2$ , 5 bar: half-surface-pressure air temperature  
 $15GMOL_{3h}half\ p.epso.315\ gmol^{-1}$ ,  $15H_2+N_2$ , 3 bar: half-surface-pressure air temperature

Figure 6.5: 10-day average temperature maps of the half-surface-pressure level for  $4.6\ gmol^{-1}$  and  $15\ gmol^{-1}$   $H_2 + N_2$  atmospheres with surface pressures of 3, 5, and 10 bar, and constant opacity  $\kappa = 22.4\ cm^2\ kg^{-1}$ . The global temperature distributions are similar but the maximum and minimum temperatures differ.

sponding to an  $H_2-N_2$  mixture with molar concentrations of 90%  $H_2$  and 10%  $N_2$ , or 50%  $H_2$  and 50%  $N_2$ . We used the same opacity  $\kappa$  in all these tests.

We will focus on the temperature of the half-pressure level, which fits the observations better in general (see Section 6.4.4). The observed high maximum brightness temperature suggests that the greenhouse gas supplying the optical thickness has a window at 4.5, as an optically thick grey-gas-like continuum would have a radiating level high in the atmosphere, which does not fit the observed high day-side temperature and large day-night contrast.

Figure 6.5 shows the temperature at the half-surface-pressure level in the tests with different surface pressures. Increasing the atmospheric pressure affects the temperature distribution as predicted in Section ??, as the day-night contrast decreases and the hot-spot shift increases (see Table 6.4). The hot-spot shift does not increase for the  $15\ gmol^{-1}$ , which may be because their higher mean molecular weight forces a very short radiative timescale even at higher surface pressures.

The  $4.6\ gmol^{-1}$ , 10 bar case is compatible with the observed phase curve maximum

*5sh<sub>2h</sub>alfp.epso.34.6 gmol<sup>-1</sup>, H<sub>2</sub>+N<sub>2</sub>,  $\tau_\infty = 2.0$ :* half-surface-pressure air temperature  
*H<sub>2</sub>N<sub>2</sub>5h<sub>alf</sub>p.epso.34.6 gmol<sup>-1</sup>, H<sub>2</sub>+N<sub>2</sub>,  $\tau_\infty = 4.0$ :* half-surface-pressure air temperature  
*5sh<sub>8h</sub>alfp.epso.34.6 gmol<sup>-1</sup>, H<sub>2</sub>+N<sub>2</sub>,  $\tau_\infty = 8.0$ :* half-surface-pressure air temperature

Figure 6.6: 10-day average temperature maps of the half-surface-pressure level for 4.6 gmol<sup>-1</sup> H<sub>2</sub> + N<sub>2</sub> atmospheres with surface pressure 5 bar and optical thicknesses of 2.0, 4.0, and 8.0.

and shift (see Section ?? for a more quantitative comparison), but has a much hotter night-side than the observations. The 5 bar case matched the observed peak shift and amplitude within error, and has a cooler night-side which is more compatible with observations (see Section 6.5.1 for a discussion of how clouds could further improve the night-side fit). Therefore, we chose the 4.6 gmol<sup>-1</sup>, 5 bar case as our “best-fit” test.

In the rest of this paper, we discuss the effect of vertical structure on the brightness temperature and phase curve. We simulate the phase curves of our tests and compare them to the observed phase curve. We will also consider which other physical processes such as cloud formation could affect the real temperatures and observed fluxes to explain the observed phase curve.

### 6.4.3 Effect of Optical Thickness

The previous section tested the effect of changing the surface pressure. We kept the atmospheric composition and opacity the same, but this meant that the optical thickness  $\tau_\infty$  changed with the surface pressure. In this section, we test the effect of changing the optical thickness with all other parameters constant, and demonstrate that the optical thickness does not greatly affect the global circulation, temperature distribution, and phase curve as discussed in Section ??.

We modelled three 5 bar  $4.6 \text{ g mol}^{-1}$  atmospheres with  $\tau_\infty = 8.0, 4.0$ , and  $2.0$ . Section ?? predicts that the optical thickness will not have a large effect on the global circulation and temperature distribution (other than on the magnitude of the temperatures). Figure 6.6 shows the temperature at the half surface pressure level for these three tests. All the tests have a similar global temperature distribution, and the tests with higher optical thickness have higher temperatures as expected. Figure ?? in the next section shows that  $\tau_\infty$  only affects the magnitude of the thermal phase curves of these tests.

The test with  $\tau_\infty = 2.0$  is not hot enough to match the observations. The test with  $\tau_\infty = 8.0$  matches the peak of the observed phase curve better than the  $\tau_\infty = 4.0$  case, but its night-side is much hotter than the observations. If the criterion was only to match the magnitude and position of the peak of the phase curve, the  $\tau_\infty = 8.0$  case would be our “best-fit”. However, in Section 6.5.1 we show that the  $\tau_\infty = 4.0$  case could also match the night-side observations given high night-side cloud formation, so we choose this to be our “best-fit” case.

#### 6.4.4 Vertical Structure

The brightness temperature measured in a thermal phase curve depends on the composition via two sets of properties. The atmospheric composition affects the radiative features which determine the heating rate, and the thermodynamic parameters affect the temperature distribution with latitude, longitude, and pressure. Finally the radiative features determine how this manifests as a brightness temperature to an observer. In this section we will discuss how the important features of the temperature distribution vary with depth

## 6.4. Results

---

Tprofiles.epso.3(a) Temperature profile for several columns around the equator of the 5 bar  $4.6 \text{ gmol}^{-1}$   $\text{H}_2+\text{N}_2$  atmosphere, with adiabats plotted in grey. dncontrast.epso.3(b) Day-night contrast versus pressure level, defined as the difference between the warmest and coolest hemispheres for consistency with ?. hotspotlocation.epso.3(c) Hot-spot shift versus pressure level for all atmospheres, up to a level where the zonal temperature gradient is too small for a distinct hot-spot shift.

Figure 6.7: Vertical structure of the tested atmospheres. The best-fit “ $\text{H}_2+\text{N}_2$ , 5 bar” case here has mean molecular weight  $4.6 \text{ gmol}^{-1}$  and  $\tau_\infty = 4.0$ . The  $T(p)$  profiles follow the dry adiabat on the lower atmosphere of the day-side, but tend towards isothermal elsewhere. The day-night contrast always increases closer to the surface. The hot-spot shift generally increases further from the surface, but becomes indistinct without a large day-night contrast.

in the atmosphere, and consider how the effect of the thermodynamic parameters can be distinguished from the effect of the radiative features on observations.

Figure 6.7a shows the temperature-pressure profiles of evenly spaced vertical columns around the equator of the planet. The planet is heated at the substellar point, where air rises through the deep convective troposphere. The global circulation discussed in Section ?? moves heat eastwards in the mid-atmosphere, generating an inversion at the east terminator due to rapid surface cooling there. This shows the importance of a GCM over 1D models to this investigation, as some profiles are greatly perturbed from radiative-convective equilibrium by the atmospheric dynamics. It also shows how features such as the day-night contrast vary with depth, as the difference between the maximum and minimum temperatures is much greater at the surface.

Figure 6.7b shows that the day-night contrast is largest low in the atmosphere. This suggests that the large observed day-night brightness temperature contrast of 1300 K may be due to emission from the lower atmosphere of the planet. This could be explained a

*phasescurves<sub>p<sub>level</sub></sub>.eps*

Figure 6.8: Phase curves for different radiating levels in the 5 bar, 4.6 gmol<sup>-1</sup>, H<sub>2</sub> + N<sub>2</sub> atmosphere. Raising the radiating level has a very similar effect to decreasing the molar mass in Figures ?? and ??, leading to a degeneracy in interpreting the observed phase curve (the black point and line show the maximum and minimum observed fluxes, with error bars).

greenhouse gas with a generally high longwave opacity to account for the high temperatures, but with a window at 4.5 so the radiating level is low in the atmosphere at this wavelength.

Figure 6.7c shows how the hot-spot shift varies with pressure level in the atmosphere. It increases with height because the heat transport is stronger higher in the atmosphere. The lower atmosphere is also strongly coupled to the surface temperature, which tends towards no hot-spot shift due to the distribution of the incoming shortwave radiation.

Figure ?? shows how the radiating level determines the observed phase curve due to the vertical structure of the atmosphere. The different phase curves correspond to the 4.5 emission from various pressure levels in the 5 bar, H<sub>2</sub> + N<sub>2</sub> atmosphere. The phase curve of the lower atmosphere has a much larger amplitude than the upper atmosphere, while the peak offset is much larger in the upper atmosphere. This corresponds to a larger day-night contrast in the lower atmosphere, and a larger hot-spot shift in the upper atmosphere. The grey-gas model OLR corresponds roughly to the 0.2 p<sub>s</sub> radiating level (see Section ??).

The fundamental degeneracy in the observations is made clear by comparing Figure ?? and Figure ???. Both show a family of curves which vary from a large amplitude curve centered on 0, to a small amplitude curve with a large offset. Increasing  $t_{rad}/t_{transp}$  by changing the composition has the same effect as observing a radiating level higher in the

## 6.4. Results

---

atmosphere.

Observations at different wavelengths could resolve these degeneracies by probing different pressure levels. For instance, it is possible that the high brightness temperatures observed are due to weaker atmospheric absorption at 4.5 than the average longwave opacity, so the measured radiation is from a lower level than the grey-gas OLR. H<sub>2</sub>-H<sub>2</sub> or H<sub>2</sub>-N<sub>2</sub> collision-induced absorption could cause this effect, as it has weaker absorption at 4.5 than on average in the thermal infrared at these temperatures (?). H<sub>2</sub>O could also fill this role, as it has strong overall thermal infrared absorption but weak absorption at 4.5 (unless it is abundant enough for self-induced continuum absorption). CO<sub>2</sub> and CO do absorb in this region, so could not be abundant if our suggestion is correct. Broadband observations would measure the overall longwave radiating level, and could be compared to the 4.5 measurements to identify an absorption window.

### 6.4.5 Mean Molecular Weight

### 6.4.6 Surface Pressure

### 6.4.7 Optical Thickness

### 6.4.8 Vertical Structure

### 6.4.9 Phase Curves

## 6.5 Simulated Observations

We simulated the 4.5 phase curves of each test to directly compare them to the observations of 55 Cnc e, and to make their amplitude and peak offset clear. These are more practically useful than the temperature maps in section ??, which show the results of the atmospheric dynamics but do not quantitatively show the amplitude and peak offset that would be observed.

The 4.5 phase curve was calculated using the weighted outgoing 4.5 spectral radiance (from the outgoing grey-gas flux brightness temperature). We integrated over the hemisphere centered on each grid cell around the equator in turn (?):

$$I_p(\xi) = \frac{\int_{-\pi/2}^{\pi/2} \int_{-\xi-\pi/2}^{-\xi+\pi/2} I_{4.5}^\uparrow|_{p=0} \cos(\lambda + \xi) \cos^2(\theta) d\lambda d\theta}{\int_{-\pi/2}^{\pi/2} \int_{-\xi-\pi/2}^{-\xi+\pi/2} \cos(\lambda + \xi) \cos^2(\theta) d\lambda d\theta} \quad (6.8)$$

for phase angle  $\xi$ , outgoing 4.5 flux  $I_{4.5}^\uparrow|_{p=0}$ , longitude  $\lambda$ , and latitude  $\theta$ .

The planetary flux  $F_p$  is compared to the stellar flux  $F_\oplus$  (?):

`phasesurveysaryp.eps`

Figure 6.9: Phase curves calculated using the emission from the half-surface-pressure level of the  $4.6 \text{ gmol}^{-1}$   $\text{H}_2 + \text{N}_2$  atmospheres with surface pressures of 3, 5, and 10 bar, corresponding to the temperature maps in Figure 6.5.

$$\frac{F_p}{F_\oplus} = \frac{I_p}{I_\oplus} \left( \frac{r_p}{r_\oplus} \right)^2 \quad (6.9)$$

for  $\frac{r_p}{r_\oplus} = 0.0187$ , and  $I_\oplus$  given an effective temperature of 5196 K (?).

Figure ?? shows the resulting phase curves for different mean molecular weight values. The maximum and minimum fluxes of the real, observed phase curve are plotted as points. It is clear that the single-gas tests do not fit the data well. Test 1 ( $\text{H}_2$ , 10 bar,  $\tau_{inf} = 8.0$ ) has a hot-spot shift, but a very flat curve due to its efficient heat circulation. Test 2 ( $\text{H}_2$ , 10 bar,  $\tau_{inf} = 8.0$ ) has a large amplitude, but no hot-spot shift due to its small radiative timescale. The phase curve of Test 5 ( $\text{H}_2+\text{N}_2$ , 5 bar,  $\tau_{inf} = 4.0$ ) fits the observations better, as does its temperature distribution in section ???. It has a large peak offset and amplitude, although not as large as the observed offset and amplitude. This discrepancy may be partly due to the high radiating level imposed by the grey-gas approximation with a high optical thickness.

Figure ?? shows the phase curves which would be measured from a radiating level at half the surface pressure for each mean molecular weight test – a possibility if the atmosphere's opacity at 4.5 is lower than its mean opacity. The  $\text{H}_2\text{-N}_2$  test fits the observations better in this figure, with a larger phase curve peak offset and amplitude than the OLR phase curve. The night-side flux is still too high, but this could be explained by cloud formation on the night-side (see Section 6.5.1).

We varied the surface pressure of the  $4.6 \text{ gmol}^{-1}$   $\text{H}_2\text{-N}_2$  case, to determine the “best-fit”

*phasescurves,s<sub>t</sub>au.eps*

Figure 6.10: Phase curves calculated using the emission from the half-surface-pressure level of the 5 bar 4.6 gmol<sup>-1</sup> H<sub>2</sub> + N<sub>2</sub> atmospheres with optical thicknesses of 2.0, 4.0, and 8.0, corresponding to the temperature maps in Figure 6.6.

to the observed phase curve (discussed in Section 6.4.2). Figure ?? shows the phase curves of the emission from the half-pressure level for the three tests. These show how increasing the pressure increases the offset and peak magnitude, but decreases the amplitude (as the opacity was constant, so the optical thickness increased). If the criterion were just to match the position and magnitude of the hot-spot shift, the 10 bar case would be the best fit. However, we chose the 5 bar case as our “best-fit” as it has the possibility to match the observations given high cloud formation on the night-side, which we discuss in Section 6.5.1.

Figure ?? shows the phase curves of the tests in Section 6.4.3, where we varied the optical thickness of the 5 bar 4.6 gmol<sup>-1</sup> H<sub>2</sub>-N<sub>2</sub> to determine its effect on the global circulation and temperature distribution. As expected, the optical thickness does not affect the global temperature distribution and phase curve, beyond the magnitude of the temperatures and fluxes.

In general, the phase curves calculated using the temperature of the half-pressure level matched observations better than those from the grey-gas OLR. The hypothetical absorption window at 4.5 discussed above could be responsible, and would also explain the high temperatures observed on the day-side. These require a high mean longwave opacity to maintain high surface temperature but a low 4.5 opacity to allow radiation from the hot layers to escape to space and account for the observed 4.5 brightness temperature.

*phasescurves<sub>f</sub>lux.eps*

Figure 6.11: Simulated 4.5 phase curves calculated from the brightness temperature of the grey-gas OLR. The red curve is the 10 bar H<sub>2</sub> atmosphere, which has such efficient heat transport that it has a large peak offset and very small amplitude. The blue curve is the 10 bar N<sub>2</sub> atmosphere, with very weak heat transport so a large amplitude and peak offset. The green curve is the 5 bar H<sub>2</sub>+N<sub>2</sub> atmosphere, with a significant offset and amplitude. The offset and amplitude are not as large as the ? measurements, shown by the black point and line (with their errors shown by the bars and the shaded area).

*phasescurves<sub>t</sub>emp.eps*

Figure 6.12: Simulated phase curves for the emission from a radiating level at half-surface-pressure. The amplitude and offset are larger than the phase curves of the OLR. The offset and amplitude are not as large as the ? measurements, but Figure ?? shows that the H<sub>2</sub>+N<sub>2</sub> atmosphere (blue curve) could match the observations with the night-side cloud formation discussed in Section 6.5.1.

To summarise, the thermal emission from the half-pressure level of the 5 bar, 4.6 gmol<sup>-1</sup> H<sub>2</sub>+N<sub>2</sub> test matched the observed phase curve peak offset and magnitude in Figure ??, but did not match the minimum flux (night-side temperature). None of the phase curves calculated with the model grey-gas OLR matched the observations, but we do not consider this to be important – in reality, the radiating level of the 4.5 emission will depend entirely on the radiative species in the atmosphere. We discuss the effect of clouds and condensables in more detail in the next section, as they could decrease the apparent night-side temperature and better explain the observations.

### 6.5.1 Condensables and Clouds

It is possible that clouds form high on the colder night-side so the photosphere there is higher and cooler. This would lead to less thermal emission from the night-side, and a

## 6.5. Simulated Observations

---

larger day-night contrast and phase curve amplitude. (?). In this section, we use a simple calculation to estimate the effect of night-side clouds on the phase curve of our  $4.6 \text{ gmol}^{-1}$ , 5 bar  $\text{H}_2+\text{N}_2$  atmosphere, which was the test with the coolest night-side which also matched the observed phase curve peak amplitude and offset.

Clouds could be formed by condensables such as SiO or Na from a day-side magma ocean. ? calculated the partial pressures of different species over magma in a vacuum at different temperatures, and showed that a magma ocean at a temperature around 2700 K (the measured mean day-side temperature) would support a significant partial pressure of multiple species, the most abundant being SiO and Na which would both have partial pressures of approximately 10 mbar. The maximum surface temperatures of our tests are over 3000 K, where SiO becomes more abundant and reaches partial pressures of hundreds of mbar.

We decided to focus on clouds at the top of the atmosphere to find the upper limit on the possible effect of clouds, as in ?. We used ? to estimate a range of surface partial pressures of SiO and Na, based on the surface temperature of the hot-spot. Then, we calculated the saturation partial pressure of SiO and Na for the highest level of each column (?). If this was larger than the surface partial pressure, we set the radiating level to the top of the atmosphere in that column, and recalculated the phase curve.

In the range of partial pressures from ?, we found that SiO could condense on the night-side of some of our tests, but that Na would not condense in any tests. Figure ?? shows that at high enough equilibrium partial pressures, the SiO clouds could significantly increase the day-night contrast and phase curve amplitude. For a partial pressure of 300 mbar, the new phase curve matches the observations of ? within error. Figure ?? also shows that at

high SiO partial pressures, heterogeneous day-side cloud formation can increase the hot-spot shift, as clouds tend to form towards the cooler western terminator on the day-side (?). This effect is small in our modelled atmospheres but might be important for different atmospheric compositions or different condensables.

Further observations at more wavelengths would be needed to find clouds on the planet, or to discover which species are present. Measuring and understanding the condensables present could help to break the degeneracies discussed in Section 6.4.4, as their concentrations could be linked to the real surface temperature via the calculations of ?. These calculations also only apply to partial pressures in a vacuum, so further work on this topic would benefit from the partial pressures outgassed into an atmosphere from a magma ocean.

In conclusion, SiO from a magma ocean is a good candidate for a cloud species which would affect observations. It could form clouds high on the night-side which would increase the phase curve amplitude, making our  $4.6 \text{ gmol}^{-1}$ , 5 bar  $\text{H}_2 + \text{N}_2$  test consistent with the observations. Future work could include a model of cloud formation and transport, which would be more realistic than our post-processing which essentially only predicts cloud formation in cold areas of the atmosphere.

## 6.6 Discussion

We can use our theory and results from sections ?? and ?? to make suggestions about the composition of an atmosphere on 55 Cnc e that would produce the observed thermal phase curve. It is important to reiterate our main assumptions that the atmosphere is composed

*phasesurfacesLOUDS.eps*

Figure 6.13: Simulated phase curves for different equilibrium surface partial pressures of SiO in the  $4.6 \text{ gmol}^{-1}$ , 5 bar  $\text{H}_2 + \text{N}_2$  atmosphere. 10 mbar corresponds to the mean day-side surface temperature, 50 mbar to the mean temperature in the region between  $25^\circ\text{N}$  to  $25^\circ\text{S}$  and  $25^\circ\text{E}$  to  $25^\circ\text{W}$ , and 100 mbar to the maximum surface temperature. The 300 mbar curve shows that clouds could form on the day-side at high enough surface partial pressures. The offset and amplitude of the 100 mbar case almost agrees with the ? measurements within error. It is not clear which partial pressure is appropriate, as the calculated pressures strictly apply to magma under a vacuum (?), and there is not a single clear magma ocean temperature in our results.

primarily of diatomic molecules and has negligible shortwave opacity. Further modelling work should investigate the effect of real-gas radiation and variable molar heat capacity.

Our best fit to the observations was the 90%-10% mixture of  $\text{H}_2$  and  $\text{N}_2$  with a mean-molecular weight of  $4.6 \text{ gmol}^{-1}$ , a specific heat capacity of  $7443 \text{ J kg}^{-1}\text{K}^{-1}$ , optical thickness 4.0, and a 5 bar surface pressure. Figure 6.3 uses the theory of ? to show that any atmosphere with a significant hot-spot shift and day-night contrast must have a similar composition to this.

The phase curve shown in Figure ?? from the OLR of this best-fitting test did not match the measured phase curve of ?, as its offset and amplitude were too small. The other tests could reproduce one of these features to be large enough, but not both at the same time. The phase curve calculated from the thermal emission of the half-pressure level in Figure ?? matched the observed phase curve peak offset and amplitude, but did not match the minimum (without night-side cloud formation).

This difference could be due to a number of things. Firstly, the model and theory might be inaccurate or overly simplified. Secondly, our parameter space of simple  $\text{H}_2$  and  $\text{N}_2$  at-

mospheres may not represent the real atmosphere. It is still possible that the main component could be a gas such as CO<sub>2</sub> with a different molar heat capacity, which is the main variable we have not investigated. Very high or low surface pressures are also possible, and might require a different modelling approach (for example, a volatile-dominated thin atmosphere).

However, we can explain the difference via other physical processes. We have discussed the effect of clouds formed by condensables, which could form on the night-side and greatly increase the phase-curve amplitude. These condensables could also affect the vertical structure and dynamics. There may be behaviour which is not captured by our grey-gas approximation, where optically active species might absorb in the shortwave or let through 4.5  $\mu\text{m}$  flux, which would affect the atmospheric structure and dynamics, and its phase curve.

Tidal heating could help to explain the observed day-side and night-side temperatures. 55 Cnc e is expected to have an eccentricity of approximately 0.001, leading to tidal heating between  $10^{-3} \text{ W m}^{-2}$  and  $10^6 \text{ W m}^{-2}$  (?, ?). Without an atmosphere, a flux of  $10^6 \text{ W m}^{-2}$  would raise the substellar temperature by 200 K, partly explaining the day-side temperature.

The 1300 K night-side temperature could also be sustained by a tidal heating flux of approximately  $10^5 \text{ W m}^{-2}$ , removing the need for an atmosphere to keep the night-side warm. However, in order for such a large flux to diffuse through a solid rock layer with typical diffusivity would require the crust to be a mere 3mm thick. A solid crust would not be stable under such circumstances, implying a global magma ocean with consequently high night-side temperature. In addition, tidal heating does not explain the observed hot-spot shift. We can speculate, however, that tidal heating could play a role in explaining the

magnitude of the observed day-side temperature, especially if transport of tidal heating to the surface favoured the partially molten day-side over the cooler night-side.

Therefore, we suggest that an atmosphere is the current best explanation for the observations. We can use our results to rule out certain atmospheres and make suggestions about a likely atmospheric composition. A single-gas, clear-sky atmosphere with only H<sub>2</sub> or N<sub>2</sub> is not consistent with the observations, as their thermodynamic properties preclude both a large phase curve amplitude and peak shift.

Our suggested climate is therefore our “best-fit” atmosphere with: mean-molecular weight of 4.6 gmol<sup>-1</sup>, specific heat capacity of 7443 Jkg<sup>-1</sup>K<sup>-1</sup>, optical thickness of 4.0, and 5 bar surface pressure. This could fit the observed phase curve given high night-side clouds and a window at 4.5 . The composition could be a 90%-10% mixture of H<sub>2</sub> and N<sub>2</sub> with some trace greenhouse gases such as CO<sub>2</sub> or H<sub>2</sub>O, and with cloud-forming species such as SiO from a day-side magma ocean.

## 6.7 Conclusions

The large hot-spot shift and day-night temperature contrast of the thermal phase curve of 55 Cnc e present a puzzle. We used theories of circulation on tidally locked planets to predict the composition of simple atmospheres on 55 Cnc e which would show either of these features. We modelled these climates, which qualitatively agreed with our predictions. We then predicted and modelled a “best-fit” composition, which had a significant hot-spot shift and day-side contrast. This atmosphere did not match the measured phase curve by itself, but could match it given high night-side clouds and an absorption win-

## 6.7. Conclusions

---

dow at 4.5 . We showed that the global circulation, temperature distribution, and thermal phase curve depends strongly on the mean molecular weight and the surface pressure. The atmospheric optical thickness and opacity does not greatly affect the global temperature distribution beyond its magnitude.

Further modelling work should include the effects of real-gas radiation, condensables, and clouds. These could all affect the atmosphere’s horizontal and vertical structure, as well as the radiating level and outgoing radiation. Shortwave absorption from atmospheric gases and clouds, heat transport by condensables, and the effect of scattering could be important to the atmospheric structure and circulation, and to the observed phase curve.

Observations at different wavelengths would be invaluable in breaking the degeneracies described in this paper. Broadband observations could reveal the overall brightness temperature of the planet, and answer the questions we have raised about a spectral window at 4.5 . Observations at other wavelengths could probe different levels of the atmosphere and be compared to the vertical structure of models such as that shown in Section ?? . These would help to solve the degeneracies between radiating level and composition that we discussed above. Further, the indications of an H<sub>2</sub>-rich atmosphere from our fit to the phase curve are problematic in view of the likely high H<sub>2</sub> escape rate from 55 Cnc e. It should be noted that it is only the hot spot phase shift that pushes the fit toward a low molecular weight atmosphere; other features could be accounted for with a high molecular weight atmosphere dominated by, e.g., N<sub>2</sub>, CO, or CO<sub>2</sub>. For future observations of this planet and other lava planets, accurate determination of the hot-spot shift is essential.

In this paper we explored the range of surface pressures from 3 to 10 bar. Very thin atmospheres (including thin rock-vapour atmospheres such as posited by (?)) are incon-

sistent with the fairly large observed night-side temperature. However, 55 Cnc e could conceivably have a much thicker atmosphere than we investigated. For an atmosphere with surface pressure of hundreds or thousands of bars, the infrared opacity of any plausible constituent would make the brightness temperature insensitive to circulation and temperature deep in the atmosphere, except insofar as the deep circulation affects the circulation in the upper atmosphere. If the upper atmosphere were to decouple dynamically from the deep atmosphere, the phase curve could become independent of surface pressure. A very massive atmosphere, however, would tend to have very high surface temperatures, and the effects on vapourisation from a probably global magma ocean might have observable consequences. The observational signature of massive atmospheres on lava planets constitutes a fruitful area for future study. This regime would require attention to the effects of atmospheric absorption of incoming stellar energy, neglected in the present study.

Some of our test runs showed transience on the scale of days in their temperature distributions, which might be detectable by future observations with high time resolution. These seemed to be caused by the cold-spot cyclones moving around the planets, and the varying jet speed and position. The 5 bar H<sub>2</sub>+N<sub>2</sub> atmosphere varied its 4.5 flux phase curve amplitude by 20% and its offset by 30% (10) over the course of ten days. This is significantly less than the variation of 400% reported by ?, but this short-period variability could be a target for future observations. For comparison, the phase curve amplitude of the H<sub>2</sub> 10 bar test only varied by a few percent over the same time period. Observations of similar variability have already been made of a hot giant planet by ?.

We set out to test whether the observed phase curve is inconsistent with the presence of an atmosphere more massive than the thin rock-vapour atmospheres typically assumed

## 6.7. Conclusions

for lava planets. We have shown that an atmosphere with 5 bar surface pressure and a mean molecular weight of  $4.6 \text{ g mol}^{-1}$  could be consistent with the observations given cloud formation high on the night-side. We hope that this paper has demonstrated how the climates of terrestrial planets can be constrained by models working closely with observations, and how suggestions can be made about the composition of their atmospheres. Similar studies should become possible for many more planets as observational and modelling capabilities improve.

## CHAPTER 7

### *Clouds on Lava Planets*

---

*“One face is forever sunlit, and one forever dark, and only the planet’s slow liberation gives the twilight zone a semblance of seasons.”*

— Stanley G. Weinbaum, *The Lotus Eaters*

Cloud-covered exoplanets are a great problem for exoplanet observers, turning illuminating spectra into flat lines. Uniform cloud cover can be an issue, but heterogenous cloud cover may be useful.

Hot Jupiters are suggested to have cloud cover. Lava planets could have

In this chapter, I address the outstanding question from Chapter X – could the difference between our model results of 55 Cancri e and the observed low night-side temperature be due to high night-side clouds? I also discuss the effect of clouds on global circulation

and on observables such as hot-spot shift.

## 7.1 Clouds on Lava Planets

### 7.2 Methods

#### 7.2.1 SOCRATES Radiative Transfer

#### 7.2.2 DIHRT Dynamical Clouds

### 7.3 Cloud-Free Simulation

#### 7.3.1 Observations

### 7.4 Simulations

#### 7.4.1 Pure CO Atmosphere

#### 7.4.2 Pure CO Atmosphere with Na

#### 7.4.3 Pure CO Atmosphere with H<sub>2</sub>O

#### 7.4.4 H<sub>2</sub> Atmosphere

### 7.5 Discussion

#### 7.5.1 Implications for Climate

#### 7.5.2 Implications for Observations

## CHAPTER 8

### *Comparing Lava Planets*

---

*“Any finite number divided by infinity is as near to nothing as makes no odds, so the average population of all the planets in the Universe can be said to be zero. From this it follows that the population of the whole Universe is also zero, and that any people you may meet from time to time are merely the products of a deranged imagination.”*

— Douglas Adams, *The Restaurant at the End of the Universe*

This thesis has focused on one planet, 55 Cancri e. In the near future, many more observations of the atmospheres of lava planets, Hot Jupiters, and other tidally locked exoplanets will be made.

In this chapter, I simulate the atmospheres of two planets which will soon be observed, K2-141b and LH dS 384b. I compare the expected phase curves, hot-spot shifts, and day-night temperature contrasts. Comparing observational features of many different planets will let us test the predictions of the simulations and simplified theories discussed in this

thesis.

## 8.1 55 Cancri e

Figure X shows a control simulation for 55 Cancri e.

## 8.2 K2-141b

Figure X shows a control simulation for K2-141b. This planet is smaller and hotter than 55 Cancri e, with a more rapid rotation rate.

## 8.3 LHS 3844b

Figure X shows a control simulation for LHS 3844b.

In this chapter, I have shown how the shallow-water theory discussed in chapter X can predict the comparative differences between observations and simulations of lava planets.

## CHAPTER 9

### *Conclusions*

---

## Bibliography

---

- Boyd, J.P. The Effects of Latitudinal Shear on Equatorial Waves. Part I: Theory and Methods. *Journal of Atmospheric Sciences*, 35(1):2236–2258, Dec. 1978.
- Boyd, J.P. *Chebyshev & Fourier Spectral Methods*. Springer, 2000.
- Demory, B.O. et al. Detection of a transit of the super-Earth 55Cancrie with warm Spitzer. *Astronomy & Astrophysics*, 533:A114, Sept. 2011.
- Demory, B.O. et al. A map of the large day–night temperature gradient of a super-Earth exoplanet. *Nature*, 532(7598):207–209, Mar. 2016.
- Hammond, M. and Pierrehumbert, R.T. Wave-Mean Flow Interactions in the Atmospheric Circulation of Tidally Locked Planets. *The Astrophysical Journal*, 869(1):65, Dec. 2018.
- Heng, K. and Workman, J. Analytical models of exoplanetary atmospheres. I. Atmospheric dynamics via the shallow water system. *Astrophysical Journal, Supplement Series*, 213(2):27, Aug. 2014.
- Iga, S.I. and Matsuda, Y. Shear Instability in a Shallow Water Model with Implications for the Venus Atmosphere. *Journal of Atmospheric Sciences*, 62(7):2514–2527, July 2005.
- Matsuno, T. Quasi-Geostrophic Motions in the Equatorial Area. *Journal of the Meteorological Society of Japan Ser II*, 44(1):25–43, 1966.
- Pierrehumbert, R.T. and Hammond, M. Atmospheric circulation of tide-locked exoplanets. *Annual Reviews, Submitted*, 2018.
- Shell, K.M. and Held, I.M. Abrupt Transition to Strong Superrotation in an Axisymmetric Model of the Upper Troposphere. *Journal of Atmospheric Sciences*, 61(2):2928–2935, Dec. 2004.

## Bibliography

---

- Showman, A.P. and Polvani, L.M. The Matsuno-Gill model and equatorial superrotation. *Geophysical Research Letters*, 37(1):L18811–n/a, Sept. 2010.
- Showman, A.P. and Polvani, L.M. Equatorial Superrotation on Tidally Locked Exoplanets. *The Astrophysical Journal*, 738(1):71, Sept. 2011.
- Thuburn, J. and Lagneau, V. Eulerian Mean, Contour Integral, and Finite-Amplitude Wave Activity Diagnostics Applied to a Single-Layer Model of the Winter Stratosphere. *Journal of Atmospheric Sciences*, 56(5):689–710, Mar. 1999.
- Tsai, S.M., Dobbs-Dixon, I. and Gu, P.G. Three-dimensional structures of equatorial waves and the resulting super-rotation in the atmosphere of a tidally locked hot Jupiter. *Astrophysical Journal*, 793(2):141, Oct. 2014.
- Vallis, G.K. Atmospheric and Oceanic Fluid Dynamics. *Atmospheric and Oceanic Fluid Dynamics*, pages 770–, Nov. 2006.
- Winn, J.N. et al. A Super-Earth Transiting a Naked-Eye Star . *The Astrophysical Journal*, 737(1):L18, Aug. 2011.

## APPENDIX A

### *Exo-FMS*

---

Three-dimensional simulations are an important tool for understanding atmospheric dynamics and climate.

A General Circulation Model (GCM)

This chapter describes my work on the GCM Exo-FMS, and discusses the specific needs and issues of the atmospheres that I simulated with it.

I will discuss the dynamical core and grid of the model

This chapter does not include much scientific investigation, but I will try to show that an exoplanet GCM is not a fanciful attempt to recreate an unknowable planet, but can be used carefully alongside basic theories and real observations to understand processes that are only apparent in a full 3D representation of the planetary atmosphere. I will also argue that XX.

## A.1 Model Structure

### GFDL-FMS

Exo-FMS is based on the cubed-sphere dynamical core of the GFDL FMS.

### Github Repository

It was very important that Exo-FMS should be openly available. I manage its Github repository and wiki.

### ExoFMS Interface

Exo-FMS is meant to make the fewest modifications to the original FMS structure and cubed-sphere dynamical core as possible. To this end, I wrote a single interface to couple the dynamical core to our physics modules (radiative transfer, convection etc.).

## A.2 Dynamics

The dynamical core of the GFDL-FMS solves the primitive equations.

For the work in Chapter 6, I used a dynamical core with a latitude-longitude grid. This grid was divided up by latitude, with each processors handling a certain number of latitude bands (three by default).

We found that the latitude-longitude grid did not deal well with instabilities at the poles of our simulations, particularly the very hot, tidally locked atmospheres under investiga-

tion. On a latitude-longitude grid, the cells get smaller and less stable towards the pole, and schemes are required to deal with cross-polar transport and instabilities. This led to the model unpredictably crashing without a particular cause.

To solve this problem, I updated the model to use a cubed-sphere grid.

A cubed-sphere grid is X.

As the version of the overall FMS system was newer for the new cubed-sphere dynamical core, it was simpler to just start again and treat it as a new model.

## A.3 Radiative Transfer

I used a semi-grey radiative transfer scheme.

## A.4 Cloud Microphysics

### A.5 Example Planets

#### A.5.1 Temperate Terrestrial Planets

#### A.5.2 Lava Planets

#### A.5.3 Gas Planets

## APPENDIX B

### *GFDL-SDC*

---

The non-linear shallow-water simulations in Chapter X were run using the Geophysical Fluid Dynamics Laboratory Spectral Dynamical Core (GFDL-SDC).

#### **B.1 Model Details**

The GFDL-SDC uses a spectral solver.

#### **B.2 Simulation Details**

I used a shallow-water variant of the GFDL-SDC, with a single layer following the shallow-water equations:

The tests in Figure X were forced by a relaxation to the height field X, the same as the linear theory in Chapter X.

The tests in Figure X also had a zonal acceleration applied with the form X, the same

---

## B.2. Simulation Details

as the tests of the linear theory in Chapter X.

## APPENDIX C

### *Pseudo-Spectral Methods*

---

In this appendix, we discuss how we solved the linearized shallow-water equations using a pseudo-spectral collocation method (Boyd, 2000). Defining a linear ordinary differential equation or system of equations:

$$Lu = q \quad (\text{C.1})$$

$L$  is a differential operator acting on the variable  $u$ , and  $q$  is the forcing or eigenvalue term. The solution is written as a sum of a series of basis functions:

$$u(x) = \sum a_n \psi_n(x) \quad (\text{C.2})$$

For a system of equations rather than a single equation,  $L$  is a matrix and  $u$  and  $q$  are vectors. We impose the condition that the differential equation is satisfied at  $N$  “collocation points”, the positions of which depend on the set of basis functions.

This is equivalent to specifying that the “residual” – the difference between the exact solution and the pseudo-spectral series solution – is zero at these points. This provides  $N$  equations to solve for the  $N$  unknowns  $a_n$ , which gives the matrix equation:

$$\mathbf{H}\mathbf{a} = \mathbf{f} \quad (\text{C.3})$$

## C.1 Solving Equations

### Solving One Equation

[Boyd \(1978\)](#) solves the linearized shallow-water equations, by reducing them to a single equation for a single variable, and applying the pseudo-spectral method. In this paper, we solve the entire system of shallow-water equations at once with the method in Appendix C.1, but explain the method for a single equation here as it naturally leads to the second method ([Boyd, 2000](#)).

The matrix elements  $H_{ij}$  in equation C.3 are evaluated using the operator  $L$  at the collocation points  $x_i$  and for every mode  $\phi_j$ , and the vector elements  $f_i$  are the terms  $q$  evaluated at the collocation points  $x_i$ :

$$H_{ij} = L\phi_j(x_i) \quad (\text{C.4})$$

$$f_i = q(x_i) \quad (\text{C.5})$$

This is then solved using a standard linear algebra routine to find  $a_n$ , and the solution

$u(x)$  is reconstructed using Equation C.2.

## Solving Systems of Equations

The pseudo-spectral method can also be applied to systems of linear ordinary differential equations. For a system of forced, time-independent equations:

$$\mathbf{Lu} = \mathbf{q} \quad (\text{C.6})$$

The condition that the differential equation is satisfied at the collocation points gives the equivalent matrix equation to Equation C.3:

$$\mathbf{Ha} = \mathbf{f} \quad (\text{C.7})$$

$\mathbf{H}$  is an  $M \times N$  square matrix with elements:

$$H_{ij}^{kl} = L^{kl} \phi_j(x_i) \quad (\text{C.8})$$

i.e. the operator  $L^{kl}$  which acts on the  $l$ th variable in the  $k$ th equation, applied to the  $j$ th basis function and evaluated at the  $i$ th collocation point.  $\mathbf{f}$  is a vector made up of  $N$  subvectors  $f_i$ , which are the forcing terms in each equation evaluated at each collocation point.

$$\mathbf{H} = \begin{pmatrix} (H_{ij} & \dots)^{kl} & \dots \\ \vdots & \ddots & \dots \\ \vdots & & \ddots \end{pmatrix} \begin{pmatrix} (\alpha_i) \\ \vdots \\ \vdots \end{pmatrix} = \begin{pmatrix} (f_i) \\ \vdots \\ \vdots \end{pmatrix} \quad (\text{C.9})$$

$\mathbf{H}$  is the same as the matrix in Equation C.4 with the elements  $H_{ij}$  replaced by sub-matrices  $H_{ij}^{kl}$ . Solving this system returns the coefficients of the basis functions, and the solutions are:

$$u(y) = \sum_{n=0}^N a_n \phi_n; \quad v(y) = \sum_{n=0}^N b_n \phi_n; \quad h(y) = \sum_{n=0}^N c_n \phi_n \quad (\text{C.10})$$

This gives a linear matrix equation with one solution corresponding to the coefficient vectors  $a_n$ ,  $b_n$ ,  $c_n$  of the forced solution.

Without forcing, the shallow-water equations define an eigensystem where the eigenvalue is the frequency  $\omega$ .

$$\mathbf{L}\mathbf{u} = \omega \mathbf{P}\mathbf{u} \quad (\text{C.11})$$

The pseudo-spectral equation is then:

$$\mathbf{H}\mathbf{a} = \omega \mathbf{R}\mathbf{a} \quad (\text{C.12})$$

$\mathbf{R}$  is an  $M \times N$  square matrix with elements:

$$R_{ij}^{kl} = P^{kl} \phi_j(x_i) \quad (\text{C.13})$$

i.e. the eigenvalue operator  $P^{kl}$  acting on the  $l$ th variable in the  $k$ th equation, applied to the  $j$ th basis function and evaluated at the  $i$ th collocation point.

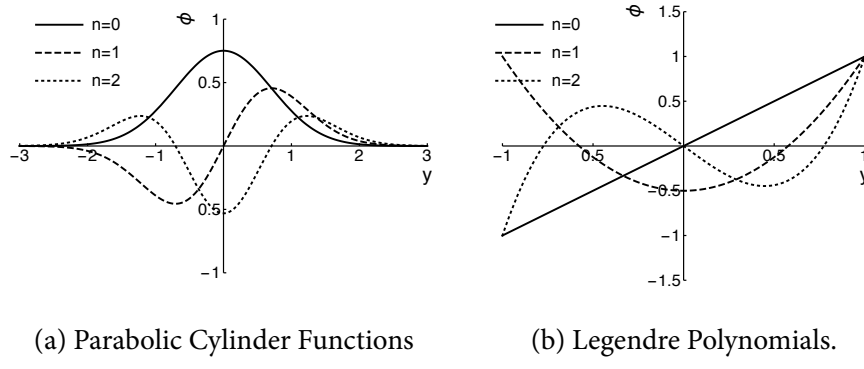


Figure C.1: Basis functions used in beta-plane and spherical coordinates.

$$\mathbf{H} = \left( \begin{pmatrix} H_{ij} & \dots \\ \vdots & \ddots \\ \vdots & \ddots \end{pmatrix}^{kl} \dots \right) \begin{pmatrix} \alpha_i \\ \vdots \\ \vdots \end{pmatrix} = \omega \left( \begin{pmatrix} R_{ij} & \dots \\ \vdots & \ddots \\ \vdots & \ddots \end{pmatrix}^{kl} \dots \right) \begin{pmatrix} \alpha_i \\ \vdots \\ \vdots \end{pmatrix} \quad (\text{C.14})$$

This gives an eigenvalue matrix equation, with  $N$  eigenvalues and eigenvectors, corresponding to the frequencies and coefficient vectors  $a_n$ ,  $b_n$ ,  $c_n$  for each free mode. Not all  $N$  modes must be physically realistic, so we identify the spurious modes by inspecting the eigenvalues for different values of  $N$ .

## C.2 Example Solutions

### Beta-plane solutions

We use the **parabolic cylinder functions**  $\psi_n(y)$  ([Showman and Polvani, 2011](#)) as defined in Equation C.15 as a basis set for the pseudo-spectral method on the beta-plane (Equation ??), as they are the exact free solutions of [Matsuno \(1966\)](#) ([Boyd, 2000](#)).

Their collocation points are at their zeros (which are just the zeros of the Hermite polynomials  $H_n$ ). Figure C.1a shows the first few **parabolic cylinder functions**.

$$\psi_n(y) = e^{-y^2/2} H_n(y) \quad (\text{C.15})$$

Figure C.2 shows the magnitude of the coefficients (Equation C.10) of the pseudo-spectral solution of the shallow-water equations linearized about a jet on a beta-plane (plotted in Figure ??). The first plot shows that when the background jet flow is zero, only modes up to  $n = 2$  are non-zero. This is the analytic solution from [Matsuno \(1966\)](#), which the pseudo-spectral method identifies because we have used the free modes (the **parabolic cylinder functions**) as our basis functions.

For non-zero jet speed (corresponding to Figure ??), the pseudo-spectral series solution does not terminate, but the coefficients for the 30th mode are about eight orders of magnitude smaller than the largest mode. The beta-plane solutions in this paper were all calculated with at least 30 modes.

## Spherical solutions

We use the Legendre polynomials as a basis set for the pseudo-spectral method in a spherical geometry (Equation ??). Figure C.1b shows the first few Legendre polynomials. Our collocation points are the zeros of these functions.

As discussed in Section ??, Equation ?? has a singularity at the poles, which we avoided by using a rescaled height  $\gamma$ , where  $\gamma = h/\cos\phi$  ([Iga and Matsuda, 2005](#)). We replaced  $h$  with  $\gamma \cos\phi$  in Equation ??, solved as normal, then multiplied the solution for

## C.2. Example Solutions

---

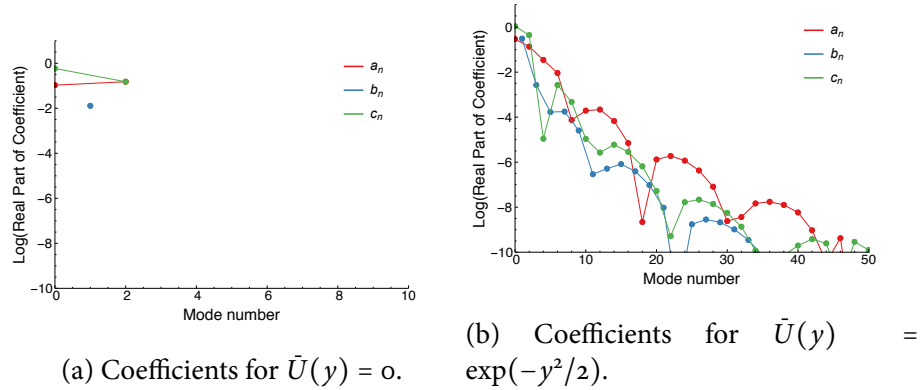


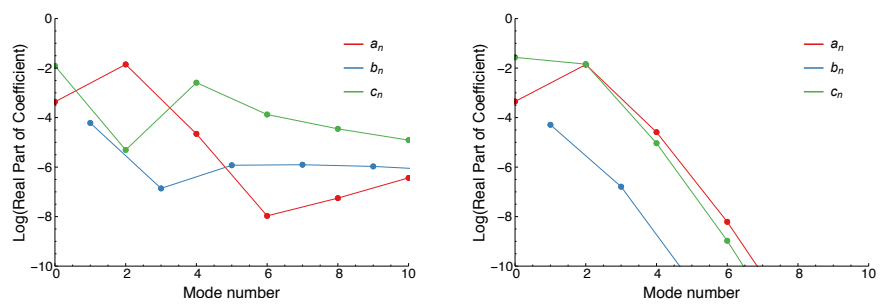
Figure C.2: Coefficients of the pseudo-spectral solution on the beta-plane coordinates with and without a background jet (the plots in Figure ??). The method identifies the exact solution in the first case, and converges rapidly to an accurate solution in the second case.

$\gamma$  by  $\cos \phi$  to recover the solution for  $h$ .

Figure C.3 shows how rescaling the  $h$  variable made the solutions converge much more quickly. In fact, the solutions without a rescaled  $h$  variable never reached a smooth solution at the poles.

## C.2. Example Solutions

---



(a) Coefficients calculated with height  $h$ . (b) Coefficients calculated with rescaled height  $y = h/\cos \phi$ .

Figure C.3: Coefficients of the pseudo-spectral solution in spherical coordinates (the first plot in Figure 3.13), with the height variable  $h$  and the rescaled height  $y = h/\cos \phi$ . Rescaling the height makes the method converge to a smooth solution at the poles.